Research
A SCIENCE PARTNER JOURNAL

RESEARCH ARTICLE

# Methanesulfonate in Phosphate Electrolyte Superstructure Enables Ampere-Hour Practical Aqueous Batteries

**Jian Zhi[1,2*†], Yunfeng Luo[2†], Chenyi Liao[3†], Zhongyi Liu[2†], Mei Han[1,2], Kaihang Yue[1], Lei Zhang[2], Guohui Li[3,4*], and P. Chen[2,5*]**

[1]State Key Laboratory of High Performance Ceramics, Shanghai Institute of Ceramics, Chinese Academy of Sciences, Shanghai 200050, China. [2]Department of Chemical Engineering and Waterloo Institute of Nanotechnology, University of Waterloo, Waterloo, Ontario N2L 3G1, Canada. [3]Laboratory of Molecular Modeling and Design, State Key Laboratory of Molecular Reaction Dynamics, Dalian Institute of Chemical Physics, Chinese Academy of Sciences, Dalian, Liaoning 116023, China. [4]Interdisciplinary Research Center for Biology and Chemistry, Liaoning Normal University, Dalian, Liaoning 116029, China. [5]School of Chemical and Biomolecular Engineering, College of Engineering, Eastern Institute of Technology, Ningbo, Zhejiang 315200, China.

*Address correspondence to: jzhi@mail.sic.ac.cn (J.Z.); ghli@dicp.ac.cn (G.L.); p4chen@uwaterloo.ca (P.C.)
†These authors contributed equally to this work.

**Citation:** Zhi J, Luo Y, Liao C, Liu Z, Han M, Yue K, Zhang L, Li G, Chen P. Methanesulfonate in Phosphate Electrolyte Superstructure Enables Ampere-Hour Practical Aqueous Batteries. *Research* 2026;9:Article 1170. https://doi.org/10.34133/research.1170

Submitted 24 November 2025
Revised 1 February 2026
Accepted 2 February 2026
Published 25 February 2026

Copyright © 2026 Jian Zhi et al. Exclusive licensee Science and Technology Review Publishing House. No claim to original U.S. Government Works. Distributed under a Creative Commons Attribution License (CC BY 4.0).

Present high-voltage Li-ion aqueous batteries largely rely on highly concentrated (up to 63 *m*) "water-in-salt" electrolyte with limited cycle life (<1,000 cycles) and little hope in practical application. To date, no dilute aqueous electrolyte (salt molality < 2 *m*) can reliably operate beyond 2 V with cycling life over 1,000 cycles. Here, we introduce a "methanesulfonate in phosphate" superstructure that simultaneously tailors $Li^+$ migration in molecular crowding solvent and electrode surfaces, which enables an unprecedented electrochemical stability window (up to 4.5 V) and cyclability (up to 10,000 cycles) in a dilute 1.1-*m* aqueous electrolyte. In addition, Such methanesulfonate in phosphate electrolyte can be also applied in various high-voltage electrode couples, and the assembled 60-V, 15-A·h $LiMn_2O_4/LiTi_2(PO_4)_3$ aqueous battery can drive an electric bike for 70 km, highlighting the power of such electrolyte design in the commercialization of high-voltage aqueous batteries.

## Introduction

As lithium-ion (Li-ion) batteries with organic electrolytes are extensively utilized in electronic devices and electric vehicles, there are increasing safety concerns due to their flammability and toxicity, rendering them unsuitable for large-scale energy storage systems [1,2]. Furthermore, the stringent moisture-free processes required for the assembly of these flammable organic electrolytes also incurred substantial manufacturing costs, thereby limiting the global production capacity of Li-ion batteries [3,4]. Replacing flammable organic electrolytes with aqueous electrolytes presents a viable strategy to address the safety issues associated with conventional Li-ion batteries and to reduce manufacturing expenses. Nevertheless, the electrochemical stability window (ESW) of aqueous electrolyte is narrow (1.23 V), which severely constrains the energy density of aqueous Li-ion batteries by limiting the range of electrode couples that can be used [5,6].

Recently, the "water-in-salt" (WIS) concept has introduced a concentrated electrolyte design that expands the ESW of aqueous electrolytes [7,8]. This approach uses a high concentration of 21-*m* lithium bis(trifluoromethanesulfonyl)imide (LiTFSI) [9], extensively utilized in aqueous batteries. The elevated salt concentration fosters the formation of a LiF-based solid electrolyte interface (SEI) through the electrochemical decomposition of the $TFSI^-$ [10], thereby extending the ESW of WIS electrolytes to approximately 3 V. Efforts to further widen the ESW include using organic imide hydrate melts of LiTFSI [11], using "water-in-bisalt" (WIBS) electrolytes with additives [12], and increasing the LiTFSI concentration to 63 *m* ($mol \cdot kg_{solvent}^{-1}$) [13]. Despite these advancements, economic and environmental concerns continue to restrict the real applications of WIS electrolytes [14]. For instance, LiTFSI salt has limited large-scale capability that is only available in small quantities at a high price of \$10 $g^{-1}$ (Sigma-Aldrich, 2022). Moreover, the use of such highly concentrated fluorinated salts normally results in extremely low ion transfer kinetics in LiF-rich interphase [15], leading to limited cycling life (<1,000 cycles ) and poor tolerance under extreme and abusive conditions [16]. To overcome these challenges, alternative strategies to develop a dilute electrolyte with enhanced ion conductions are urgently required to make aqueous batteries feasible in large-scale energy storage systems.

It is well known that dilute electrolytes normally show a low ionic conduction because the scarcity of ions limits total charge transport, which has been often quoted to be detrimental in battery performance [17]. However, we argue the opposite and believe through precise solvent shell reconfiguration; the ion transfer kinetics can still be enhanced in dilute aqueous electrolyte. Inspired by molecular crowding electrolyte design proposed by Xie et al. [18], here, we reported "methanesulfonate in phosphate" (MIP) liquid superstructure that enables increased $Li^+$ transference number ($t_{Li+}$) and diffusion coefficient ($D_{Li+}$) in a dilute (1.1 *m*) lithium methanesulfonate (LiMS) aqueous electrolyte compared to their concentrated counterparts (18 *m*). Such peculiar trend is realized by the synergic superionic pairing between trimethyl phosphate (TMP) and methanesulfonate ($MS^-$) anions. In one hand, bulky methyl phosphate groups from TMP spatially shield $Li^+$–$H_2O$ interactions and cut off the widely extended Li–MS interaction network, which leads to an increased degree of uncorrelation between $Li^+$ and $MS^-$ motions and a higher calculated $t_{Li+}$ and $D_{Li+}$. In another hand, the oxygen atoms from strongly polarized $-SO_3^-$ of $MS^-$ carry a high negative charge and form strong ion–dipole interactions with the $H^+$ atoms in $H_2O$ molecules. Such $H_2O$–$H_2O$ hydrogen bond (HB) disruption results in a smaller and more dynamic solvation shell, faster solvation exchange, and reduced competition from proton conduction—together leading to enhanced $Li^+$ transport kinetics.

Meanwhile, we also identified a selective diffusion of $Li^+$ over $H^+$ at the γ-$Li_3PO_4$ and amorphous $Li_3PO_4$ electrode–electrolyte interfaces derived from such MIP electrolyte superstructure. This unique feature markedly suppresses oxygen and hydrogen evolution in dilute aqueous electrolyte while maintaining excellent $Li^+$ transfer kinetics, which enables an exceptional lifespan (up to 10,000 cycles) in full batteries and widened ESW (up to 4.5 V) that even surpasses the ESW (3 V) of concentrated WIS electrolytes. This work is a notable departure from the previously reported LiF-rich electrode–electrolyte interphase based on organic additives and $TFSI^-$ anions, which only physically blocks $H_2O$ to improve interfacial stability in aqueous electrolytes [18–20]. Our MIP electrolyte design also demonstrates a high output voltage (up to 2.5 V) in a wide range of battery systems, including $LiMn_2O_4$ (LMO)/$LiTi_2(PO_4)_3$ (LTP), LMO/$TiO_2$, LMO/$Li_4Ti_5O_{12}$ (LTO), LMO/$Zn_2Nb_{34}O_{87}$ (ZnNbO), $LiCoO_2$ (LCO)/LTO, $LiNi_{0.33}Co_{0.33}Mn_{0.33}O_2$ ($NCM_{111}$)/LTO, and $LiNi_{0.5}Co_{0.2}Mn_{0.3}O_2$ ($NCM_{523}$)/LTO. Moreover, MIP aqueous electrolytes also provide wide operating temperature range (−40 to 25 °C) and superior cycling performance (>88% capacity retention after 1,000 cycles) in 2-A·h class pouch battery, demonstrating excellent practical viability. On the basis of such ampere-hour level battery pack, we also assembled 60-V, 15-A·h aqueous battery and drive an electric bike for 70 km, highlighting the potential of MIP electrolyte in replacing lead–acid batteries in low-speed vehicles.

## Results and Discussion

Attributing to the unique nontoxic and water-miscible features of TMP [21,22], in this study, we successfully prepared a series of aqueous MIP electrolytes with TMP concentration of up to 1.13 g·$ml^{-1}$ (Table S2). The ionic conductivity of the electrolyte decreases from 20.3 to 0.9 mS·$cm^{-1}$, as the TMP concentration increases from 0 g·$ml^{-1}$ in 18-*m* LiMS–$H_2O$ to 1.13 g·$ml^{-1}$ in 0.8-*m* LiMS–TMP–$H_2O$ (Fig. S1), which is consistent with the general expectations for dilute electrolytes [23]. However, we noted an increase in both transference number ($t_{Li+}$) and diffusion coefficient ($D_{Li+}$; see Supplementary Discussion and Figs. S2 and S3) in various MIP electrolytes with increasing TMP content (from 18-*m* LiMS–$H_2O$ to 1.1-*m* LiMS–TMP–$H_2O$), peaking at 1.1 *m* and slightly declining upon further TMP increase in the 0.8-*m* electrolyte (Fig. 1A). We also calculate $D_{Li+}$ of various MIP electrolytes via pulsed field gradient nuclear magnetic resonance according to the Stejskal–Tanner equation [24]. As shown in Fig. S4, the 1.1-*m* LiMS–TMP–$H_2O$ electrolyte shows the highest $D_{Li+}$ among all MIP electrolytes, which is in good correlation with the value of $D_{Li+}$ based on galvanostatic intermittent titration technique (Fig. 1A). The sharp spectrum for 1.1-*m* LiMS–TMP–$H_2O$ (Fig. S5) indicates the averaging of the dipole and quadrupole couplings due to the isotropic fast $Li^+$ transfer kinetics that is similar to the $Li^+$ motion behavior in single crystals [25].

Such a peculiar trend in $Li^+$ diffusion kinetics implies a boosting effect in MIP electrolyte, which prompts us to investigate the intermolecular solvation structure. The Raman spectra of the 1.1-*m* LiMS–TMP–$H_2O$ electrolyte, shown alongside those of pure TMP and $H_2O$ in Fig. 1B, indicate the quenching of fluorescence, facilitated by the excited-state strengthened intermolecular HB between the phosphate groups of TMP and $H_2O$ molecules [26]. Compared to pure $H_2O$, there is a notable blue shift of the O–H stretching vibration bands in Fourier transform infrared (FT-IR) spectra of the 1.1-*m* LiMS–TMP–$H_2O$ aqueous electrolyte (Fig. 1C). It is due to the higher Gutmann donor number of TMP (23) compared to $H_2O$ (18) [27], which leads to a deshielding in the solvation sheath of $Li^+$. In addition, the red shift of P═O stretch band pairs (1,277 and 1,268 $cm^{-1}$) observed in Fig. 1D suggests the formation of an ionic-liquid-type equilibrium state with reduced activity [28,29], where $H_2O$ molecules are bonded to the phosphate groups of TMP. It is well known that FT-IR spectra is primarily based on the vibrational modes of covalent bonds such as stretching and bending vibrations, etc. [30]. These vibrational modes absorb infrared radiation and induce transitions between vibrational energy levels, forming characteristic absorption peaks. However, since $Li^+$ ions form ionic bonds rather than covalent bonds, they do not contribute to vibrational energy transitions and therefore do not produce absorption peaks in the FT-IR spectra. As a result, the presence of $Li^+$ ions does not influence the observed spectra, and there are no obvious differences between the 1.1-*m* LiMS–TMP–$H_2O$ electrolyte and the TMP–$H_2O$ solution under the same TMP:$H_2O$ molar ratio (Fig. S6).

Density functional theory (DFT) characterization was also performed to elaborately scrutinize the interplay among $MS^-$ anions and water in MIP electrolyte. As shown in Fig. S7, $MS^-$–$H_2O$ shows a binding energy of 98.26 kJ·$mol^{-1}$, which is more than 4-fold higher than that of $H_2O$–$H_2O$ (23.67 kJ·$mol^{-1}$) and much higher than those of other chaotropic anions ($TFSI^-$, $BF_4^-$, and $ClO_4^-$) with water. The HBs of water can be broken by anions through charge-driven formation of anion–H bonding; typically, a higher binding energy indicates stronger bond formation [31,32]. This effect was further examined via $^1H$ nuclear magnetic resonance spectroscopy of pure water, 1.1-*m* LiMS–$H_2O$ and 1.1-*m* LiTFSI–$H_2O$ (Fig. S8). Notably, the $^1H$ peak shifts upfield in the presence of $MS^-$ anions, confirming a weakening of the HB in water molecules, which aligns with the DFT calculations. In contrast, the degree of peak shift with

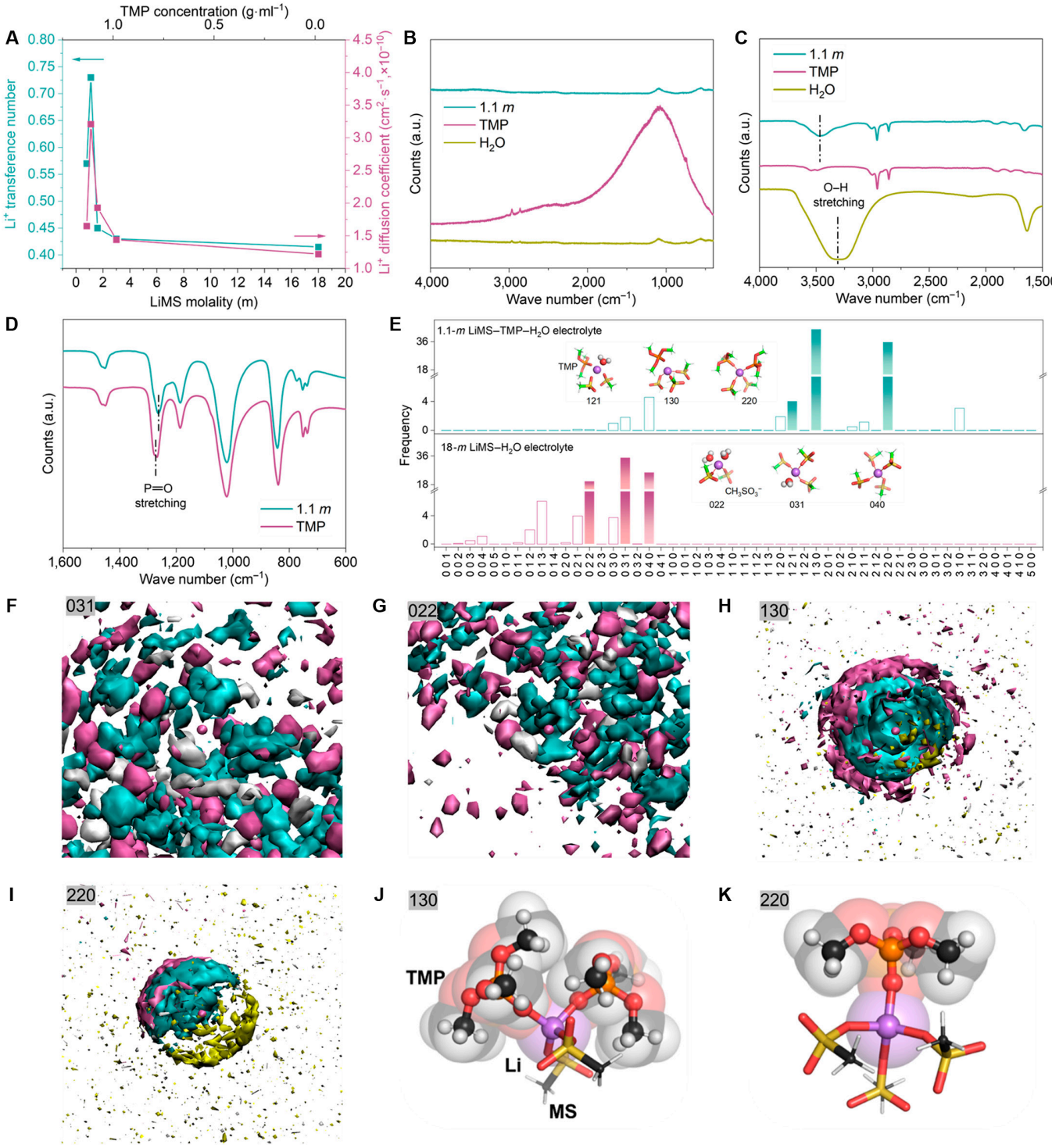



**Fig. 1.** (A) $Li^+$ transference number ($t_{Li+}$) and diffusion coefficient ($D_{Li+}$) of various LiMS–$H_2O$ electrolytes under different LiMS modalities and TMP concentrations. (B) Raman and (C and D) FT-IR spectra of 1.1-*m* LiMS–TMP–$H_2O$ electrolyte in comparison with pristine TMP and $H_2O$ solvent. a.u., arbitrary units. (E) Distribution of coordination structures between $Li^+$ and TMP, MS, and $H_2O$. (F to I) SDFs of MS (cyan), TMP (yellow), and $H_2O$ (gray) around a $Li^+$ (purple) in (F) 031, (G) 022, (H) 130, and (I) 220 coordination structures. The surfaces represent isosurfaces of normalized concentration for mass center of different components. (J and K) Molecular shielding of umbrella-shaped TMP with LiMS in (J) 130 and (K) 220 coordination structures.

$TFSI^-$ anion is relatively minor, demonstrating a weak breaking effect of HB in water.

Molecular dynamics (MD) simulations were carried out to further elucidate the solvation structures of 18-*m* LiMS–$H_2O$ and various MIP electrolytes (3.0-, 1.6-, 1.1-, and 0.8-*m* LiMS–TMP–$H_2O$). A snapshot of lithium aggregates from 18-*m* LiMS–$H_2O$ (Fig. S9) illustrates that one MS coordinates with 3 $Li^+$, which are coordinated by surrounding MS and $H_2O$ to form a wide spreading –Li–MS– matrix with dominant 040, 031, and 022 coordination structures (Fig. 1E and

Fig. S10; where "*xyz*" represents the numbers of TMP [*x*], $MS^-$ [*y*], and $H_2O$ [*z*] around one $Li^+$ atom). Spatial distribution functions (SDFs) of MS (cyan) and $H_2O$ (gray) around a $Li^+$ in a 040 configuration display a densely packed –Li–MS–$H_2O$ interaction network (Fig. S11), which becomes slightly scattered in 031 and 022 configurations (Fig. 1F and G). This result is consistent with our radial distribution function (RDF) analysis (Fig. S12), which shows that the RDF intensity for $MS^-$ is approximately 3 times higher than that of $H_2O$ due to the stronger interactions between the negatively charged oxygen atoms in $MS^-$ and $Li^+$. A similar trend is also observed in MIP electrolytes. As the TMP concentration increases, the RDF intensity of $MS^-$ gradually decreases but remains approximately twice that of TMP in the 1.1- and 0.8-*m* MIP systems. Electrolyte (1.1 *m*) predominantly features 130 and 220 ion clusters (Fig. 1E and Fig. S10), and their corresponding SDFs reveal discrete features as a colloidal solution (Fig. 1H and I).

This distinct behavior is attributed to the solvent shell reconfiguration of umbrella-shaped TMP molecules, which spatially shields $Li^+$–$H_2O$ interactions by bulky methyl phosphate groups (Fig. 1J and K) and cuts off the widely extended Li–MS interaction network (Fig. S13). Thus, compared with the extended Li–MS interaction network in the 18-*m* LiMS–$H_2O$ electrolyte, the 1.1-*m* LiMS–TMP–$H_2O$ electrolyte exhibits TMP-wrapped ion clusters, leading to an increased degree of uncorrelation between $Li^+$ and MS motions (Fig. S14 and Table S3) and a higher calculated $t_{Li+}$ (Table S2). Meanwhile, The –PO–$CH_3$ structure in TMP also provides a proper nonpolar and polar amphiphilic structure to balance TMP's solubility in MIP electrolyte by comprehensive interactions with $Li^+$ and $H_2O$ molecules. It should be noted that the $t_{Li+}$ in Table S3 is calculated from molecular simulations trajectories based on a concentrated solution theory [33], and the uncertainty for $t^+$ can be affected by the studied systems, theory approximation, the reference frame (such as center-of-mass choice for the whole box or the solvent), and the thermostat method that was applied during the MD simulations. Despite these variations, the computational data remain consistent with the experimental findings in most respects (Fig. 1A), particularly in demonstrating the higher $Li^+$ transference number of the 1.1-*m* LiMS–TMP–$H_2O$ system compared to the 18-*m* system. In addition, the oxygen atom from O═P of TMP molecules also forms abundant HB with neighboring $H_2O$ molecules (Fig. S15), substantially constraining the dynamics of H atoms and reducing water activity (Fig. S16). The more positive interaction energies of 130 and 220 structures than those of 040, 031, and 022 (Fig. S17) demonstrate the efficient mitigation of Li–MS interactions by TMP molecules and energetically improve the kinetics of uncorrelated $Li^+$ motion. Figure S18A shows the ionic conductivity of 1.1-*m* LiMS–TMP–$H_2O$ electrolytes from 25 to 70 °C. Notably low activation energy of 0.28 eV was calculated on the basis of Arrhenius equation (Fig. S18B), which is in line with the value of other highly conductive aqueous electrolyte and suggests an efficient $Li^+$ transport [34].

The enhanced $Li^+$ transfer kinetics in MIP electrolyte increase the probability of $Li^+$ in the vicinity of electrode surface, which leads to an interfacial chemistry dominated by the intimate reaction between $Li^+$ and TMP. Quantum mechanics (QM) calculations (Fig. S19) reveal that the reduction potential of TMP with Li (3.62 to 3.96 V versus Li/$Li^+$) is substantially higher than that of TMP without Li (0.89 to 1.6 V versus Li/$Li^+$). Although the standard reduction potential seems much higher than other studied material values [9], it is noted that it highly depends on the reduced products and represents the tendency under the standard condition. A high reduction potential for an initial TMP-derived product promotes rapid formation of a phosphate interface on the anode. Further analysis indicates that TMP–Li exhibits a stronger electron-accepting tendency compared to $H_2O$, thereby suppressing $H_2$ evolution (2.63 V). This preferential reduction of TMP over $H_2O$ was also validated by projected density of states (PDOS) analysis for both 18-*m* LiMS–$H_2O$ and 1.1-*m* LiMS–TMP–$H_2O$ systems (Fig. S20). In the 18-*m* LiMS–$H_2O$ system, $H_2O$ and MS contribute to the lowest unoccupied molecular orbital (Fig. S20A and B), facilitating rapid $H_2O$ reduction at the anode. In contrast, TMP from the 1.1-*m* LiMS–TMP–$H_2O$ system causes a downshift of the orbital levels and accounts for the vast majority of the lowest unoccupied molecular orbital; thus, it is predominantly reduced at the anode to form a solvent-derived interphase. In addition, TMP alters the electron density states near the highest occupied molecular orbital levels (Figs. S20C and D and S21), which may induce the formation of a solvent derived interphase on the cathode.

The growth of such interphase derived from MIP electrolyte was further characterized by cryo-transmission electron microscopy (cryo-TEM; Fig. 2A), which clearly illustrates the morphological evolution of the SEI during cycling on an LTP anode from an LMO/LTP battery with the 1.1-*m* LiMS–TMP–$H_2O$ electrolyte. After 50 cycles, the LTP anode is fully covered with a 20-nm-thick monolithic SEI, whose 2-dimensional lattice fringe matches well with the (220) interplanar spacing of γ-$Li_3PO_4$ (orthorhombic, Joint Committee on Powder Diffraction Standards #15-0760) [35,36]. High-resolution TEM further shows the growth of crystalline/amorphous $Li_3PO_4$ layer during cycling on the LMO cathode (Fig. 2B), indicating the formation of monolithic cathode–electrolyte interphase (CEI). To verify the phosphatic characteristics of this interfacial layer, we performed the x-ray photoelectron spectroscopy (XPS) depth analysis on the SEI layer of LMO/$TiO_2$ battery under the 1.1-*m* LiMS–TMP–$H_2O$ electrolyte (Fig. 2C and D). The most obvious distinction of $TiO_2$ anode cycled in this electrolyte is the existence of P arising from TMP. Etching this surface by $Ar^+$ shows that the concentration of P diminishes from the surface toward the bulk, implying that phosphorus species are mainly at the top surface of the $TiO_2$ anode (Fig. 2D). Closer examination shows a sudden decrease in $TiO_2$-related species (Ti 2p) after $Ar^+$ etching for 240 s, which remains constant even after prolonged (1,920 s) sputtering (Fig. 2C). Notably, no S 2p signal is detectable in the cycled $TiO_2$ (Fig. S22), underscoring a different trend in the changes of P 2p and Ti 2p, which undoubtedly confirm the existence of a monolithic crystalline/amorphous $Li_3PO_4$ interphase on the $TiO_2$ anode. Furthermore, energy-dispersive x-ray spectroscopy line scans (Fig. S23) and mappings (Fig. S24) clearly suggest a uniform spatial distribution of P element on the surface of $TiO_2$ anode. We wish to emphasize that the identification of $Li_3PO_4$ does not imply it is the sole phosphorus-containing component. In fact, the broad P 2p peak observed in the XPS depth profile, with its peak broadening, suggests the possible coexistence of multiple phosphorus species in diverse chemical environments, which likely includes the organic phosphate decomposition products. TEM results provide further support that while $Li_3PO_4$ was identified in the crystalline regions, amorphous areas could well contain additional components with organic phosphate groups (Fig. 2A

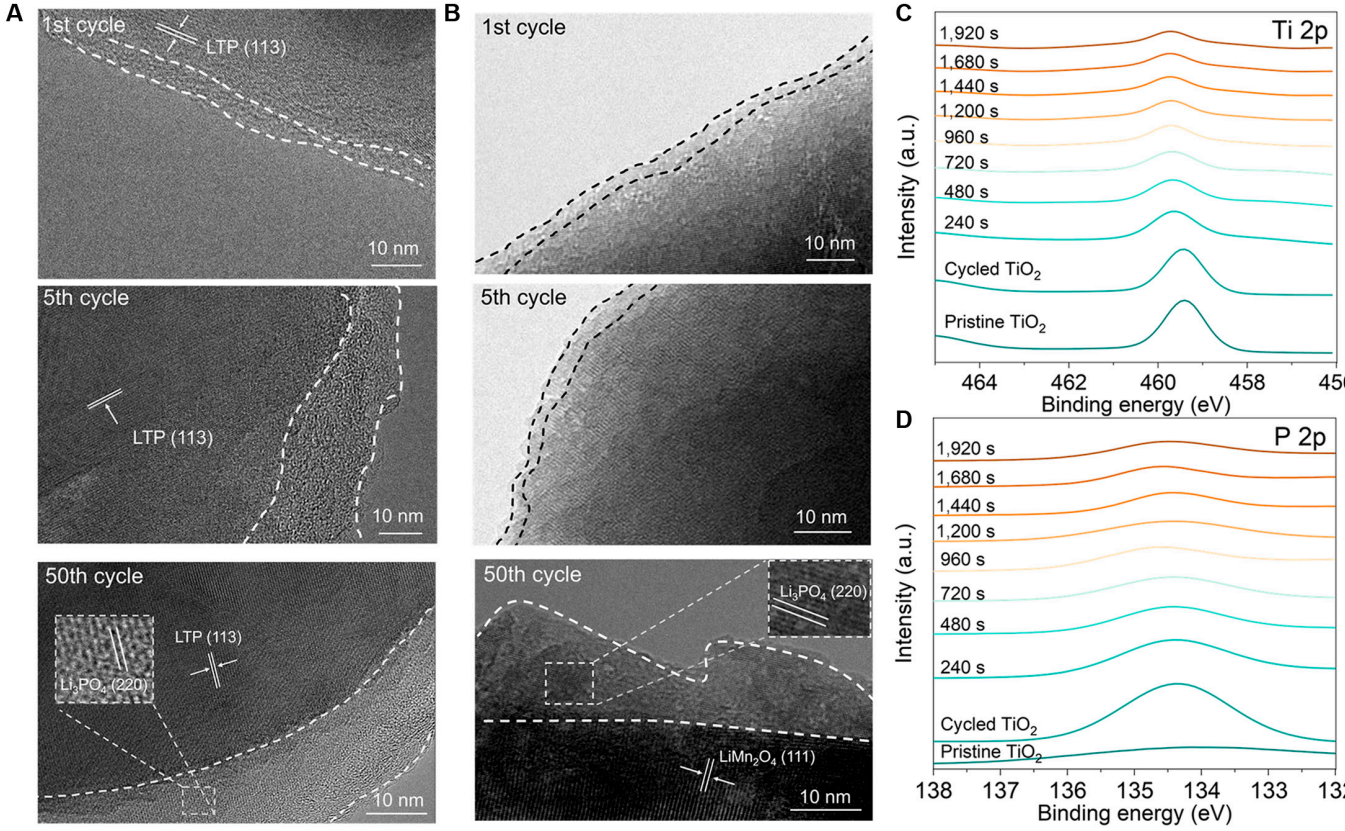



**Fig. 2.** (A) High-resolution cryo-TEM of LTP anode from LMO/LTP battery with 1.1-*m* LiMS–TMP–$H_2O$ electrolyte after 1st, 5th, and 50th cycles. (B) High-resolution cryo-TEM of LMO cathode from LMO/LTP battery with 1.1-*m* LiMS–TMP–$H_2O$ electrolyte after 1st, 5th, and 50th cycle. (C and D) XPS spectrum of Ti 2p (C) and P 2p (D) from pristine (bottom) and cycled $TiO_2$ anode after various $Ar^+$ sputtering durations.

and B). These findings collectively reinforce the view that the CEI/SEI constitutes a complex mixture.

To investigate the kinetics of $Li^+$ diffusion through such γ- and amorphous $Li_3PO_4$ SEI, we used the electrochemical impedance spectroscopy (EIS) to assess the interfacial resistance of various cycled $TiO_2$ anodes in a 3-electrode cell utilizing a 1-*m* $Li_2SO_4$ aqueous electrolyte. The Nyquist plot of the $TiO_2$ anode from the LMO/$TiO_2$ battery with a 1.1-*m* LiMS–TMP–$H_2O$ electrolyte after 50 cycles (Fig. 3A) reveals high- and medium-frequency semicircles corresponding to the SEI resistance ($R_{sei}$) and charge transfer resistance ($R_{ct}$), respectively (Fig. 3A). Utilizing an equivalent circuit model (Fig. S25), the $R_{sei}$ of the $TiO_2$ anode cycled under the 1.1-*m* LiMS–TMP–$H_2O$ electrolyte remains stable at approximately 322 Ω after 50 cycles, substantially lower than that observed for $TiO_2$ anodes operated under 1.1-*m* LiTFSI–$H_2O$ and LiTFSI–TMP–$H_2O$ electrolytes (Fig. 3B). Evidently, the $Li_3PO_4$-based SEI derived from the LiMS–TMP–$H_2O$ electrolyte exhibits more consistent $Li^+$ conduction compared to the fluorinated SEI formed in LiTFSI-based electrolytes. In addition, a higher $Li^+$ and lower $H^+$ conductivity in γ-$Li_3PO_4$ compared to LiF pellets under various hydraulic pressures (Fig. 3C) suggests faster $Li^+$ and slower $H^+$ conduction in $Li_3PO_4$ compared to LiF.

To further examine whether the $Li^+/H^+$ conduction selectivity observed in pellet samples can be transferred to thin interphases, we fabricated a series of ultrathin γ-$Li_3PO_4$ and LiF pellets with thicknesses down to 350 μm. As shown in Fig. S26A, all ultrathin γ-$Li_3PO_4$ pellets exhibit higher ionic conduction for $Li^+$ than for $H^+$. In contrast, all micrometer-scale LiF pellets display comparable $Li^+$ and $H^+$ ionic conductivities across the entire thickness range (Fig. S26B), which is consistent with the results obtained from millimeter-scale LiF pellets (Fig. 3C). These results indicate that, within the pellet thickness range down to 350 μm, the $Li^+/H^+$ selectivity of γ-$Li_3PO_4$ and LiF is insensitive to thickness under our testing conditions. To better approximate the space charge environment and interfacial conditions encountered during real battery operation, we first attached all γ-$Li_3PO_4$ and LiF pellet samples to glass fiber separators wetted with 1.1-*m* LiMS–TMP–$H_2O$ and LiTFSI–$H_2O$ electrolytes prior to the conductivity measurements. As a result, these measurements demonstrate the intrinsic $Li^+/H^+$ conduction preference of γ-$Li_3PO_4$ and the nonselective ionic transport behavior of LiF under electrolyte-wetted conditions, thereby providing strong experimental support for understanding the ionic selectivity of γ-$Li_3PO_4$- and LiF-based interphases formed from LiMS–TMP–$H_2O$ and LiTFSI–$H_2O$ electrolytes. While nanoscale interphases may additionally be influenced by space charge effects and interfacial microstructural features, the present results establish a reliable bulk reference for interpreting $Li^+/H^+$ transport behavior in the corresponding nanometer-scale interphases.

The selective ionic conduction of $Li^+$ over $H^+$ facilitated by the $Li_3PO_4$ interphase impedes the migration of $H^+$ to the bulk electrode, thereby suppressing $H^+$ from accepting electrons and subsequently inhibiting $H_2$ evolution. This conclusion is further supported by the analysis of hydrogen evolution reaction (HER) via in situ gas chromatography during the charge–discharge process of LMO/$TiO_2$ full batteries. As depicted in

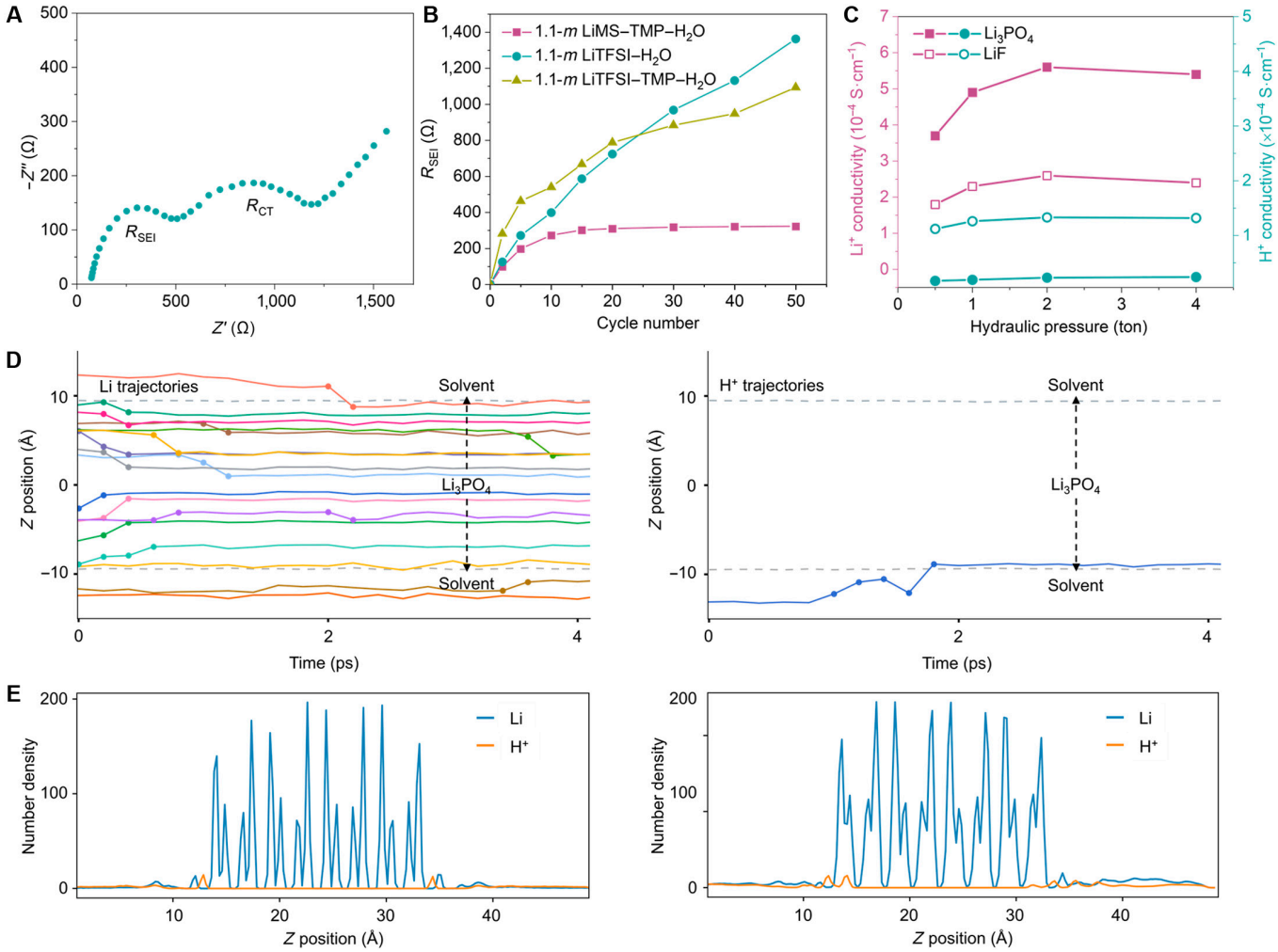



**Fig. 3.** (A) Nyquist plot of $TiO_2$ anode from the cycled LMO/$TiO_2$ battery (after 50 cycles) with 1.1-*m* LiMS–TMP–$H_2O$ electrolyte. (B) The change of $R_{sei}$ as a function of cycling number of $TiO_2$ anode from LMO/$TiO_2$ battery with 1.1-*m* LiMS–TMP–$H_2O$ electrolyte. The change of $R_{sei}$ from $TiO_2$ anode operated under 1.1-*m* LiTFSI–$H_2O$ and 1.1-*m* LiTFSI–TMP–$H_2O$ electrolyte is also shown for comparison. (C) $Li^+$ and $H^+$ conductivities of γ-$Li_3PO_4$ and LiF pellets under various hydraulic pressures. (D) Illustrations of $Li^+$ (left) and $H^+$ (right) transport trajectories in γ-$Li_3PO_4$ slabs with vacant Li sites during MD simulations. Each diffusion that is greater than 0.9 Å in 0.2 ps is marked by dots. The positions of the upper and lower interfaces of $Li_3PO_4$ slabs are marked by 2 gray dashed lines. (E) Number density of $Li^+$ and $H^+$ from 0.25-Å slices on *z* axis in γ-$Li_3PO_4$ slabs without (left) and with (right) vacant Li sites during MD simulations.

Fig. S27, LMO/$TiO_2$ batteries with a 1.1-*m* LiMS–TMP–$H_2O$ electrolyte exhibit the lowest $H_2$ evolution rate of 0.27 μmol·$h^{-1}$ during cycling at 5 C, whereas those with 1.1-*m* LiTFSI–$H_2O$ and LiTFSI–TMP–$H_2O$ electrolytes display $H_2$ evolution rates of 0.98 and 0.87 μmol·$h^{-1}$, respectively.

MD simulations on γ-$Li_3PO_4$ and amorphous $Li_3PO_4$ slabs, with and without vacant Li sites, were conducted to investigate the preference of $Li^+$ over $H^+$ diffusion tailored by the $Li_3PO_4$ interphase. Rapid $Li^+$ transport between vacant sites was observed in both γ-$Li_3PO_4$ (left of Fig. 3D) and amorphous $Li_3PO_4$ (left of Fig. S28) during "vacancy refilling" processes (Movie S1), while only proton trapping by phosphate groups at the interface was observed for $H^+$ (right of Fig. 3D and Fig. S28). Rapid $Li^+$ transport occurs at the initial stages of a "vacancy refilling" process, slowing down as the potential difference diminishes with vacant sites refilled. Figure S29 illustrates the observed $Li^+$ transport pathway between vacant sites in γ-$Li_3PO_4$, wherein $Li^+$ was capable of hopping from one vacant site to the next (approximately 3 Å) within 0.2 ps (at a rate of 15 Å·$ps^{-1}$), accompanied by interstitial motions. Figure S30 illustrate MD-equilibrated structures of γ-$Li_3PO_4$ and amorphous $Li_3PO_4$ slabs in an aqueous solution of mixed hydrochloric acid (HCl) and lithium chloride (LiCl). In a "vacancy refilling" process, vacant Li sites were generated by randomly removing lithium ions from the central slab (yellow in Fig. S30), followed by system relaxation over 100 ps repeated over 50 times. The number density of $Li^+$ and $H^+$ along the normal direction of γ-$Li_3PO_4$ slabs without (left of Fig. 3E) and with vacant Li sites (right of Fig. 3E) clearly indicates $H^+$ trapping at the surface layer, which is consistent with amorphous $Li_3PO_4$ slabs (Fig. S31). The preference for $Li^+$ transport over $H^+$ transport in $Li_3PO_4$ is attributed to the high energy barrier for $H^+$ to escape from the strong HBs of H–$OPO_3$ with a preferred H–O distance close to 1 Å (Fig. S32). Conversely, $Li^+$ can more easily transport among vacant sites (approximately 3 Å) with Li–O distance around 2 Å.

MIP electrolyte with other TMP analogs, including dimethyl methylphosphonate (DMMP) and triethyl phosphate (TEP), also shows a substantial increase in $t_{Li+}$ and $D_{Li+}$ with the increase in phosphate concentration (Fig. S33A and B), indicating the similar boosting effect of $Li^+$ migration kinetics as TMP. Under the

same LiMS:phosphate:$H_2O$ molar ratio as 1.1-*m* LiMS–TMP–$H_2O$, the $R_{sei}$ of the $TiO_2$ anode cycled under 0.9-*m* LiMS–TEP–$H_2O$ and 1.3-*m* LiMS–DMMP–$H_2O$ electrolytes remains constant after 50 cycles (Fig. S34A), indicating a stable $Li^+$ transfer kinetics on anode surface. In addition, LMO/$TiO_2$ battery using 0.9-*m* LiMS–TEP–$H_2O$ and 1.3-*m* LiMS–DMMP–$H_2O$ electrolytes exhibits much lower $H_2$ evolution rate compared to the 1.1-*m* LiTFSI–$H_2O$ electrolyte (Fig. S34B), clearly indicating the impeded $H^+$ migration on phosphate-based SEI derived from the reduction of TEP and DMMP.

Such $Li_3PO_4$-tailored $Li^+$ conduction and hindrance of $H^+$ migration at the electrode–electrolyte interface by $Li_3PO_4$ effectively enhance the overpotential of HER and oxygen evolution reactions (OERs) by preventing $H_2O$ from the bulk electrolyte, thereby extending the cathodic/anodic limits of the electrolyte. As illustrated in Fig. 4A, the overall ESW of various MIP electrolyte expands with increasing TMP concentration, pushing the gas ($O_2$ and $H_2$) evolution voltages well beyond the electrochemical stability limits of $H_2O$. Further examination of Fig. 4A reveals a negative shift in the $H_2$ evolution voltage from 1.8 V in an 18-*m* LiMS–$H_2O$ electrolyte to 0.8 V in a 0.8-*m* electrolyte (Fig. S35A). The cathodic current at 1 V decreases from $5.1 \times 10^{-3}$ mA in the 18-*m* LiMS–$H_2O$ electrolyte to $7.2 \times 10^{-5}$ mA in the 0.8-*m* electrolyte (Fig. S35B), possibly due to the passivation of the $Li_3PO_4$-based SEI. In addition, the monolithic CEI (Fig. 2F to H) with sluggish $H^+$ conductions blocks HO*, O*, and HOO* intermediate on cathode surface from the bulk electrolyte, which contribute to the suppressed OERs as evidenced by the reduced anodic current above 5.0 V. Overall, an ESW of approximately 4.5 V is achieved in 0.8, 1.1, and 1.6-*m* MIP electrolytes (Fig. 4B), with both cathodic (~1 V versus $Li/Li^+$) and anodic (~5.2 V versus $Li/Li^+$) potentials exceeding those of pure water (cathodic, ~2.63 V versus $Li/Li^+$; anodic, ~3.86 V versus $Li/Li^+$) and other dilute and concentrated aqueous

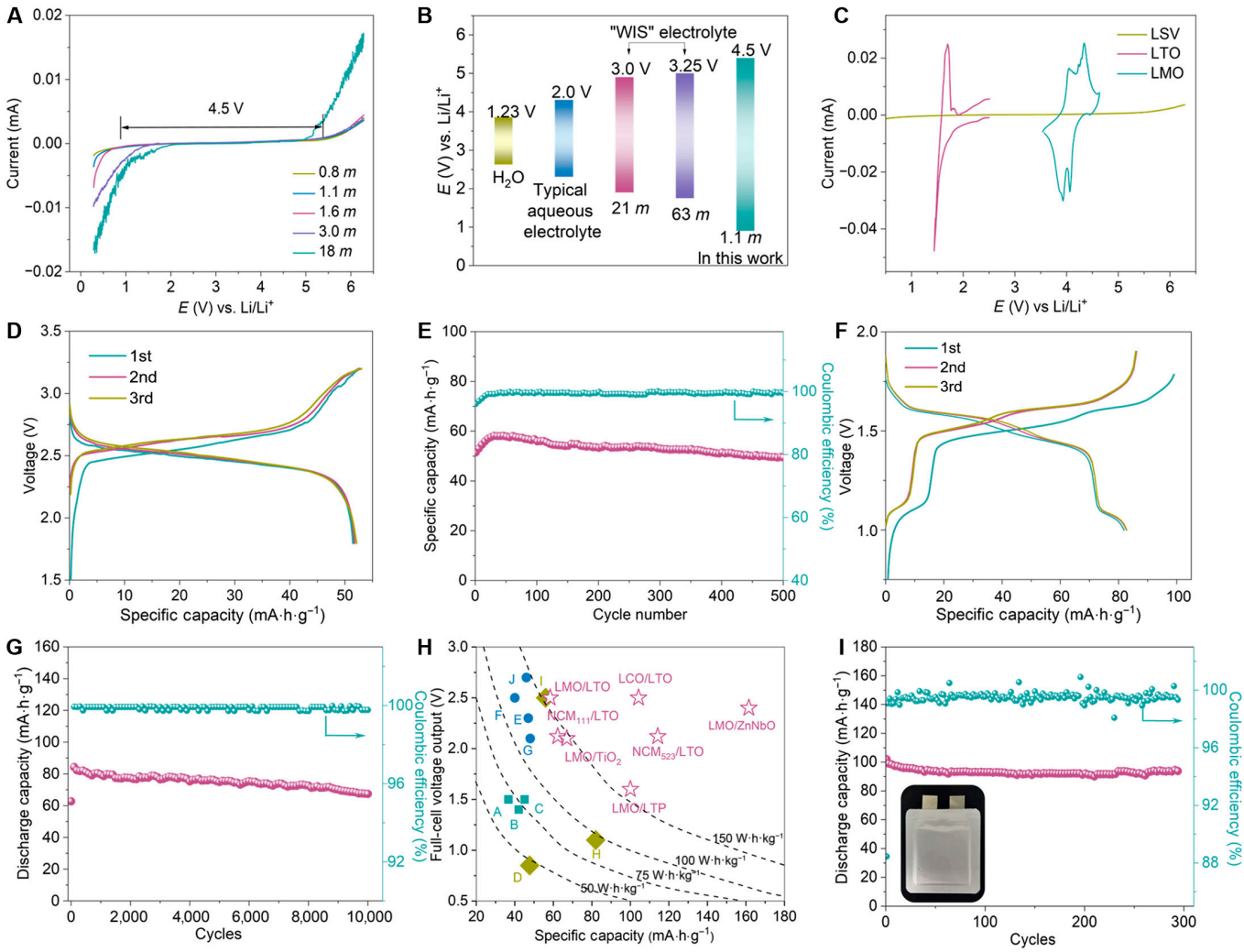



**Fig. 4.** (A) Overall ESW of 0.8-, 1.1-, 1.6-, and 3-*m* LiMS-TMP $H_2O$ and 18-*m* LiMS–$H_2O$ electrolyte. (B) Electrolyte stability window (with a scan rate of 5 $mV \cdot s^{-1}$) of 1.1-*m* LiMS–TMP–$H_2O$ electrolyte in this work, pure $H_2O$, and various aqueous electrolytes with different salt concentrations (traditional dilute aqueous electrolyte [106], 21 *m* [9], 28 *m* [52], and 63 *m* [13]). (C) ESW of 1.1-*m* LiMS–TMP–$H_2O$ electrolyte overlaid with cyclic voltammograms of LMO/LTP couple at 0.2 $mV \cdot s^{-1}$. (D) Voltage profile and (E) cycling performance of LMO/LTO aqueous battery with 1.1-*m* LiMS–TMP–$H_2O$ electrolyte at 5 C. (F) Voltage profile at 0.5 C and (G) cycling performance at 5 C of LMO/LTP aqueous battery with 1.1-*m* LiMS–TMP–$H_2O$ electrolyte. (H) Average output voltage of aqueous full cells with specific capacity based on different electrochemical couples under 1 C (A [50], B [51], C [51], D [71], E [9], F [72], G [52], H [73], I [13], and J [23]). Different colors represent different operation times during cycling: orange, below 100 h; blue, 100 to 1,000 h; green, above 1,000 h. (I) Cycling performance of 100-mA·h LMO/LTP pouch battery with 1.1-*m* LiMS–TMP–$H_2O$ electrolyte under 0.5 C. Inset shows the picture of the pouch cell. Please note that all the capacities in this manuscript are based on the mass of anode materials.

electrolytes (Fig. 4B). We further investigated the ESW of MIP electrolyte at various scan rates. In line with previous report [37], the scan rate had only a minor effect on the slope of current versus *E* curve and onset of electrolyte decomposition (Fig. S36), highlighting the robustness of the electrolyte's performance. To fundamentally avoid subjective bias introduced by arbitrarily setting a current density threshold, we innovatively used an objective determination method based on differential calculations in this study. Specifically, instead of relying on a fixed current density threshold value to identify the onset of decomposition, we performed differentiation on the measured linear sweep voltammetry curves and located the zero-crossing points of the differential curves to objectively determine the onset potentials for oxidation and reduction decomposition. The difference between these 2 onset potentials is taken as the measured ESW. As shown in Fig. S37, the ESW measured using this method is approximately 4.5 V, covering a potential range from about 1.0 to 5.5 V (versus $Li^+$/Li).

With its low cost and high stability, LTO has been widely utilized as an anode material in Li-ion batteries with organic electrolytes. However, its low $Li^+$ intercalation potential greatly limits its application in most aqueous electrolytes, even in high-concentration WIS electrolytes. This challenge can be overcome by MIP electrolyte design. The cyclic voltammogram of LMO/LTO demonstrates that the reversible lithiation/delithiation of LMO and LTO occurs within the cathodic limits of a 1.1-*m* LiMS–TMP–$H_2O$ electrolyte (Fig. 4C), enabling the full utilization of $Li^+$ intercalation/deintercalation sites that seem unattainable in other dilute aqueous solutions. The wide ESW of such an electrolyte can also accommodate the redox potentials of LMO/LTP (Fig. S38) and LMO/$TiO_2$ (Fig. S39).

Because of the wide ESW of the 1.1-*m* LiMS–TMP–$H_2O$ electrolyte, the LMO/LTO aqueous battery can operate with a high average discharge voltage of 2.5 V and a high discharge capacity of 52 mA·h·$g^{-1}$ at 5 C (Fig. 4D). Breaking $H_2O$–$H_2O$ HB networks by the introduction of $MS^-$ anion also inhibits $H^+$ transport and suppresses the water decomposition process [38], which enable aqueous batteries to deliver an exceptional cycling performance. As shown in Fig. 4E, LMO/LTO aqueous battery demonstrates excellent stability with a capacity retention of over 96% and a high coulombic efficiency of approximately 99.90% after 500 cycles. In contrast, the capacity of the LMO/LTO aqueous battery with a 1.1-*m* LiTFSI–TMP–$H_2O$ electrolyte rapidly decreases from 85 mA·h·$g^{-1}$ to only 10 mA·h·$g^{-1}$ with a low coulombic efficiency of 47% after 300 cycles (Fig. S40). It is reported that $TFSI^-$ anions are unstable toward $OH^-$ species generated from $H_2$ evolution reaction and a fluorinated SEI is eventually formed during cycling [39], which leads to a notably increasing $R_{sei}$ and poor cycling stability due to the impeded $Li^+$ migration. We also performed cycling tests of LMO/LTO aqueous batteries using 0.8-, 1.1-, 1.6-, and 3-*m* LiMS–TMP–$H_2O$ and 18-*m* LiMS–$H_2O$ electrolytes (Fig. S41). Notably, the 1.1-*m* electrolyte demonstrated superior cyclability under 3 C compared to all other LiMS–TMP–$H_2O$ electrolytes, experimentally indicating the rationality in the selection of 1.1-*m* LiMS concentration. In sharp contrast, LMO/LTO aqueous batteries using 18-*m* LiMS–$H_2O$ electrolyte quickly decayed within 180 cycles, further suggesting the necessity of TMP in retaining excellent cycling lifespan. Differential electrochemical mass spectrometry, an in situ analytical method, was used to track gas evolution in cycled cells as a function of TMP concentration. Figure S42 displays the differential electrochemical mass spectrometry collected from LMO/LTO full cells during the 151st charging process after 150 cycles at 5 C. Consistent with expectations, the TMP-free electrolyte (18-*m* LiMS–$H_2O$) exhibited predominant water splitting during charging above 3.2 V, yielding high $H_2$ and $O_2$ evolution rates of 63 and 17 nmol·$min^{-1}$ (Fig. S42A). However, raising the TMP concentration effectively inhibited this process, with decomposition at the cathode surface being more curbed than at the anode. Specifically, $O_2$ almost completely disappears at 3.0 *m* (Fig. S42B), while small amount of $H_2$ still generates at the 1.6-*m* LiMS–TMP–$H_2O$ electrolyte (Fig. S42C). The distinction between $H_2$ and $O_2$ evolution rate aligns with the well-established understanding that the kinetics of $H_2$ evolution are more favorable than those of $O_2$ evolution [40], and the root cause for the gradual capacity decay in 1.6- and 3-*m* LiMS–TMP–$H_2O$ electrolytes (Fig. S41) comes from the inevitable parasitic hydrogen evolution flux on anode surface. At 1.1 *m*, there is no detectable $H_2$ and $O_2$ evolution during the 151st charging process from LMO/LTO cells (Fig. S42D), indicating the fully suppression of $H_2O$ decomposition during cycling and ensuring a stable capacity retention after 500 cycles (Fig. 4E).

The LMO/LTP and LMO/$TiO_2$ aqueous batteries with a 1.1-*m* LiMS–TMP–$H_2O$ electrolyte also deliver high output voltages of 1.6 V (Fig. 4F) and 2.1 V (Fig. S43), respectively. By adding 20 cycles of low-rate (0.5 C) charge–discharge before the cycling test, the LMO/LTP aqueous battery can be stably operated for up to 10,000 cycles at 5 C with a capacity retention of 77% (Fig. 4G). The cycling life at 0.5 and 1 C of such a battery with a 1.1-*m* LiMS–TMP–$H_2O$ electrolyte is also verified by third-party testing (Fig. S44). The charge–discharge platforms of the LMO/LTP full cell for the 100th, 200th, and 300th cycles remain consistent, further indicating the excellent cycling stability of the system (Fig. S45). We also utilized the LMO/LTP electrode pair to evaluate the rate performance of the 1.1-*m* LiMS–TMP–$H_2O$ electrolyte. As illustrated in Fig. S46, the specific capacities of the battery under various current densities were approximately 84 mA·h·$g^{-1}$ at 0.5 C, 82 mA·h·$g^{-1}$ at 1 C, 79 mA·h·$g^{-1}$ at 2 C, 72 mA·h·$g^{-1}$ at 5 C, and 56 mA·h·$g^{-1}$ at 10 C. These data clearly indicate that the battery maintains considerable capacity output across a broad range of current densities from 0.5 to 10 C. Furthermore, after undergoing high-rate testing at 10 C, the capacity retention returned to 100% upon reverting to 0.5 C, fully demonstrating its excellent rate performance. We further compared the performance of the LMO/LTP electrode pair in our work with studies using other aqueous electrolytes, including WIS electrolytes, conventional $Li_2SO_4$ dilute electrolyte, and saturated $Li_2SO_4$ electrolytes (Fig. S47). The comparison revealed that at lower charge–discharge current densities (1 and 2 C), the performance of our battery was comparable to that of these alternative aqueous electrolytes. However, at higher current densities (5 and 10 C), our battery exhibited substantially higher specific capacities [41–45], further evidencing the enhanced $Li^+$ transfer kinetics in the 1.1-*m* LiMS–TMP–$H_2O$ electrolyte. LMO/LTP aqueous battery maintains excellent cycling stability and high coulombic efficiency at 40 and 50 °C (Fig. S48). However, at 60 °C, a sudden decline in cycling stability and coulombic efficiency is observed. This is attributed to the decomposition of TMP molecules at elevated temperatures, which leads to the release of phosphorus-containing gases that absorb energy and contributes to performance loss in cycling stability [46–49].

It is widely recognized that increasing the output voltage from aqueous batteries typically leads to a significant compromise in cycling stability, even when using WIS electrolytes [50,51]. Apparently, MIP electrolyte enables us to overcome such voltage/cycling trade-offs and achieve high values in both aspects in LMO/LTO, LMO/LTP, and LMO/$TiO_2$ battery systems (Fig. 4H). Moreover, the electrolyte demonstrates exceptional compatibility with a diverse range of battery systems, extending but not limited to LMO/ZnNbO (Fig. S49), LCO/LTO (Fig. S50), $NCM_{111}$/LTO (Fig. S51), and $NCM_{523}$/LTO configurations (Fig. S52), with the highest output voltage of 2.5 V (LCO/LTO) and a specific capacity of 161 mA·h·$g^{-1}$ (LMO/ZnNbO) at 1 C (Fig. 4H). The corresponding cycling performance of LMO/$TiO_2$, LMO/ZnNbO, LCO/LTO, $NCM_{523}$/LTO, and $NCM_{111}$/LTO full cells are presented in Fig. S53. $TiO_2$ (Fig. S53A) and ZnNbO (Fig. S53B) anodes exhibit slightly higher specific capacities and superior cycling stability in comparison with previous reports [52,53]. For LCO (Fig. S53C) whose application is traditionally limited by side reactions in aqueous systems, our electrolyte system enables it to achieve a specific capacity similar to prior reports while improving cycling stability [54,55]. However, NCM electrodes (Fig. S53D and E) show reduced cycling retention, likely due to the dissolution of Ni ions in the aqueous electrolyte, a well-known issue for ternary cathodes in aqueous systems [56]. Clearly, LMO/LTO (ceiling discharge voltage of 2.5 V) and LMO/LTP (ceiling discharge voltage of 1.5 V) show much better cycling performance (Fig. 4E and G) than LMO/$TiO_2$, LMO/ZnNbO, LCO/LTO, $NCM_{111}$/LTO, and $NCM_{523}$/LTO (Fig. S53) with 1.1-*m* LiMS–TMP–$H_2O$ electrolyte. As a result, LMO/LTO and LMO/LTP are recommended electrode couples for the practical application of LiMS–TMP–$H_2O$ electrolyte in grid-scale energy storage systems that are sensitive in lifespan. It should also be noted that the primary contribution of this work lies in proposing an electrolyte design strategy that expands the ESW, thereby offering a potential solution for high-voltage electrode pairs and verifying its basic compatibility across different material systems. Therefore, the results stated here are strictly based on the fundamental electrochemical performance data we presented when applying the electrolyte with various electrode pairs. We do not intend to claim, nor have we claimed, that this electrolyte can universally address all specific degradation challenges faced by high-voltage cathode materials.

We also fabricated a 100-mA·h LMO/LTP pouch battery with a 1.1-*m* LiMS–TMP–$H_2O$ electrolyte. The full cell (cathode [35 mg·$m^{-2}$] and anode [20 mg·$m^{-2}$] with a positive/negative electrode capacity ratio [P/N] of 1.73) can sustain over 300 cycles at 0.5 C with a capacity retention of 93% and a coulombic efficiency of 99.97% (Fig. 4I). Our pouch cell achieves a high energy density comparable to state-of-the-art systems (Fig. S54), whether evaluated by real gravimetric energy density (40 and 43.4 W·h·$kg^{-1}$ excluding the battery casing) [53,57,58] or electrode material mass (165 W·h·$kg^{-1}$) [59–70]. In addition, our pouch cell demonstrates outstanding cycling stability, maintaining excellent performance over 300 cycles (Table S4). It is important to note that aqueous batteries and organic electrolyte-based Li-ion batteries differ fundamentally in their application focus and technological pathways. Traditional high-energy-density Li-ion batteries (200 to 250 W·h·$kg^{-1}$) are primarily designed for consumer electronics and electric vehicles, where energy-to-weight ratio is extremely sensitive. In contrast, this aqueous battery system is developed with priority on intrinsic safety, environmental friendliness, low cost, and long cycle life. It targets applications such as large-scale energy storage and low-speed electric vehicles where absolute weight and volume constraints are relatively relaxed, but stringent requirements exist for safety, cost, and cycling durability.

In traditional aqueous batteries, severe water consumption, cell swelling, and significant capacity degradation occur during overcharging or deep discharging due to increased $H_2/O_2$ evolution under these abusive conditions [71,72]. Surprisingly, this issue is mitigated in the aqueous battery with MIP electrolyte. When overcharged to 2.5 V in each cycle at 0.5 C (Fig. S55), the LMO/LTP battery with 1.1-*m* LiMS–TMP–$H_2O$ electrolyte shows over 95% capacity retention with 98.26% coulombic efficiency after 85 cycles (Fig. 5A). Similar cycling performance is observed in the cell discharged to 0 V at 0.5 C (Fig. 5B and Fig. S56), indicating the safety advantage of such an electrolyte during practical operations. The excellent deep discharge and overcharge performance of such a battery are further confirmed by third-party institute testing (Fig. S57). To more intuitively demonstrate the intrinsic safety of the battery, we also supplemented nail penetration and short-circuit tests of LMO/LTP battery pack with 1.1-*m* LiMS–TMP–$H_2O$ electrolyte. The video (Movie S2) clearly documents that during these extreme abuse conditions, the battery showed no deformation, smoking, ignition, or explosion, and no thermal runaway occurred. This directly confirms its excellent safety performance.

The effective disruption of $H_2O$–$H_2O$ HB networks by $MS^-$ anions greatly increases the "tetrahedral entropy" of $H_2O$ molecules, which lowers the freezing point of water [38] and enables much higher ionic conductivity over −60 to +20 °C (Fig. S58) than the electrolytes with other lithium salts (LiTFSI, $LiClO_4$, and $LiBF_4$). Compared to the LiMS–$H_2O$ electrolyte that solidifies at −40 °C, the 3.0-, 1.6-, and 1.1-*m* LiMS–TMP–$H_2O$ electrolytes remain liquid (Fig. 5C). Because of the antifreezing property of such electrolyte, the LMO/LTP battery with 1.1-*m* LiMS–TMP–$H_2O$ electrolyte can operate at 0.2 C over a wide temperature range (−40 to 25 °C; Fig. 5D; with corresponding charge–discharge curves shown in Fig. S59). This battery also demonstrates nearly 100% capacity retention after 100 cycles at −20 °C (inset of Fig. 5D).

LiMS is a low-cost salt derived from the neutralization of LiOH and $CH_3SO_3H$ in distilled water [73]. TMP is also an inexpensive compound widely used in electroplating and textile manufacturing as a flame retardant [37,38]. As a result, the bill of materials (BOM) cost of 1.1-*m* LiMS–TMP–$H_2O$ electrolyte (Fig. 5E) is only 0.41% of a 21-*m* WIS electrolyte [9], 0.35% of a 28-*m* WIBS electrolyte [30], and 1.2% of a recently reported 4.5-*m* LiTFSI–KOH–$CO(NH_2)_2$–$H_2O$ electrolyte [14] and is close to that of a sulfate-based aqueous electrolyte (2 M $ZnSO_4$/1 M $Li_2SO_4$) used in aqueous LMO/Zn batteries [39]. Considering other factors such as safety, cycling performance, ESW, working temperature range, and abuse tolerance, it is anticipated that such an electrolyte design is superior to state-of-the-art commercial or laboratory-scale aqueous technologies, such as lead–acid, Ni–Cd, LMO/Zn, and "WIS" batteries (Fig. 5F). The low BOM cost of such MIP electrolyte also encourages us to fabricate scaled-up ampere-hour class aqueous batteries. As shown in Fig. 5G, 2-A·h LMO/LTP aqueous battery based on MIP electrolyte exhibits >98% capacity retention over 1,000 cycles while maintaining an average coulombic efficiency of ~99%. For further practical application, we also assembled a 60-V, 15-A·h commercial LMO/LTP aqueous battery using MIP electrolyte (Fig. 5H), which drives an electric bike to

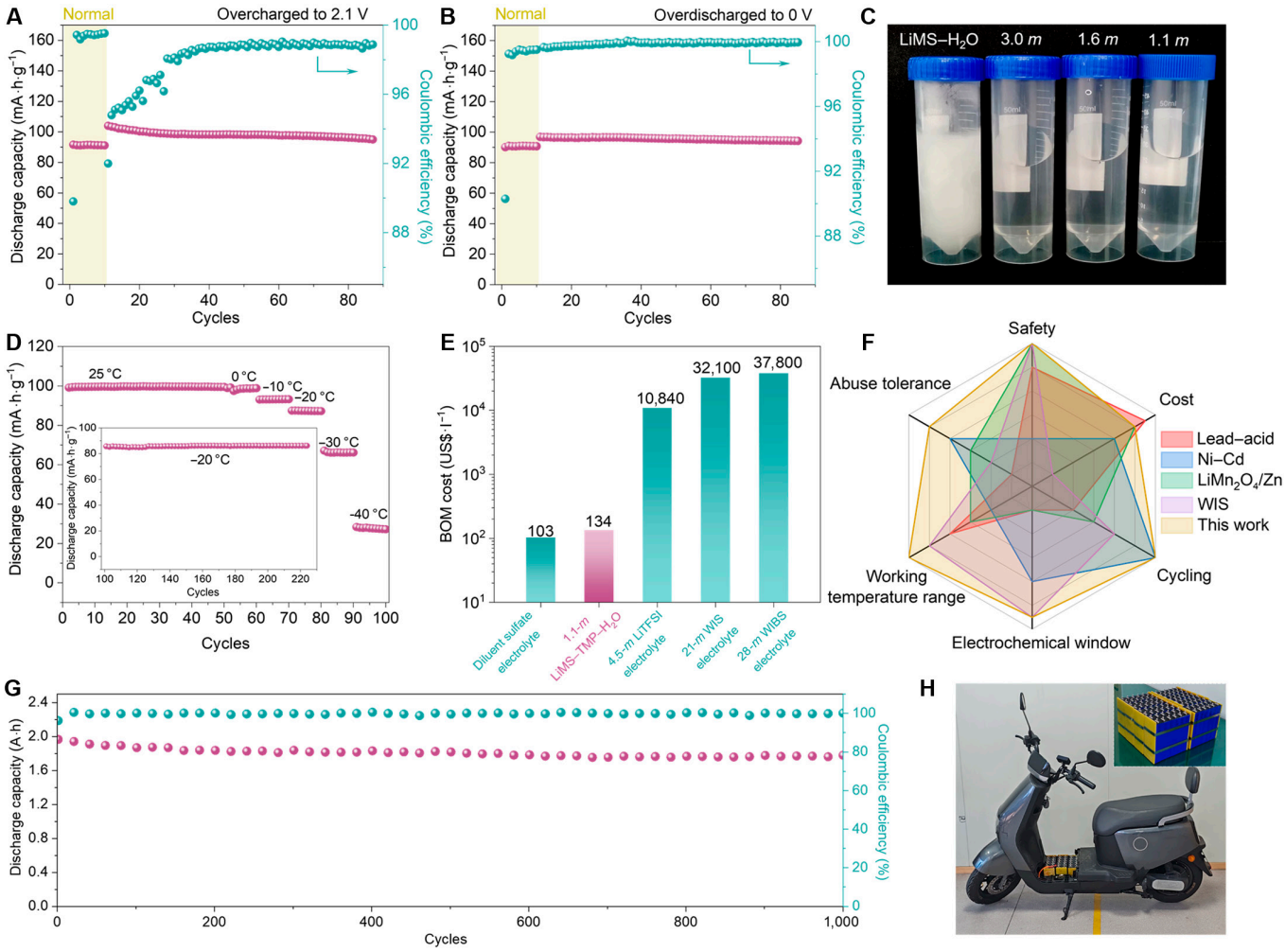



**Fig. 5.** (A) Overcharged and (B) overdischarged performance of LMO/LTP battery with 1.1-*m* LiMS–TMP–$H_2O$ electrolyte. (C) Optical photographs of LiMS–$H_2O$ electrolyte and 1.1-, 1.6-, and 3.0-*m* LiMS–TMP–$H_2O$ electrolytes at −30 °C. (D) Discharge capacity (at 0.2 C) of LMO/LTP battery with 1.1-*m* LiMS–TMP–$H_2O$ electrolyte under various working temperature (−40 to 25 °C). Inset shows the cycling performance of this battery at 0.2 C under −20 °C. (E) BOM cost comparison of 1.1-*m* LiMS–TMP–$H_2O$ electrolyte with dilute sulfate electrolyte (2 M $ZnSO_4$/1 M $Li_2SO_4$) in aqueous LMO/Zn batteries, 4.5-*m* LiTFSI electrolyte [LiTFSI–KOH–$CO(NH_2)_2$–$H_2O$], 21-*m* WIS electrolyte, and 28-*m* WIBS electrolyte. (F) Comparison of 1.1-*m* LiMS–TMP–$H_2O$ electrolyte-based batteries with other state-of-art commercial or laboratory-scale aqueous battery technologies, such as lead–acid, Ni–Cd, LMO/Zn, and "WIS" batteries. (G) Cycling performance of 2-A·h LMO/LTP pouch battery with 1.1-*m* LiMS–TMP–$H_2O$ electrolyte under 1 C. (H) Practical demonstration of the assembled commercial LMO/LTP aqueous battery with 1.1-*m* LiMS–TMP–$H_2O$ electrolyte in electric bike. The energy consumption metric of the battery is 60 V and 15 A·h.

run smoothly for a demonstration distance of 70 km (Fig. S60) and underscores its significant potential in replacing environmentally toxic lead–acid batteries in low-speed vehicles.

## Conclusion

In summary, we have identified simultaneously boosted liquid and interfacial $Li^+$ conduction in an aqueous electrolyte due to the synergic superionic pairing between TMP and $MS^-$ anions in MIP electrolyte (Fig. 6). On one hand, the phosphate group carries 3 nonpolar alkyl groups (–$CH_3$) while exposing an oxygen site to coordinate with $Li^+$. Such amphipathic structure exhibits a bulky nonpolar region and a single coordination site, functioning like an umbrella that shields $Li^+$ from extensive interactions with $MS^-$ anions in the electrolyte and thereby enhancing their migration efficiency. In another hand, strongly polarized –$SO_3^-$ from $MS^-$ form strong ion–dipole interactions with $H^+$ in $H_2O$ molecules. It leads to a smaller and more dynamic solvation shell, faster solvation exchange, and reduced competition from proton conduction—further promoting $Li^+$ transport kinetics. Meanwhile, we also observed a selective diffusion of $Li^+$ over $H^+$ in electrode–electrolyte interfaces, which is due to the trapping of proton by phosphate groups and facilitated "vacancy refilling" $Li^+$ diffusion processes in $Li_3PO_4$-based CEI and SEI. Such $Li^+$-conducting and $H^+$-impeding interfacial chemistry blocks $H^+$ transfer to the anode and oxygen-based intermediates (HO*, O*, and HOO*) to the cathode, simultaneously suppressing interfacial HER and OER (Fig. 6) and enabling a series of aqueous electrolytes with a wide ESW (up to 4.5 V) and an exceptional lifespan (up to 10,000 cycles). More importantly, this MIP electrolyte design is applicable in a wide range of battery systems, including LMO/LTP, LMO/$TiO_2$, LMO/LTO, LMO/ZnNbO, LCO/LTO, $NCM_{111}$/LTO, and $NCM_{523}$/LTO configurations, with a high output voltage (up to 2.5 V) and remarkable temperature adaptability. Attributing to its low BOM cost that is only 0.41% of the widely

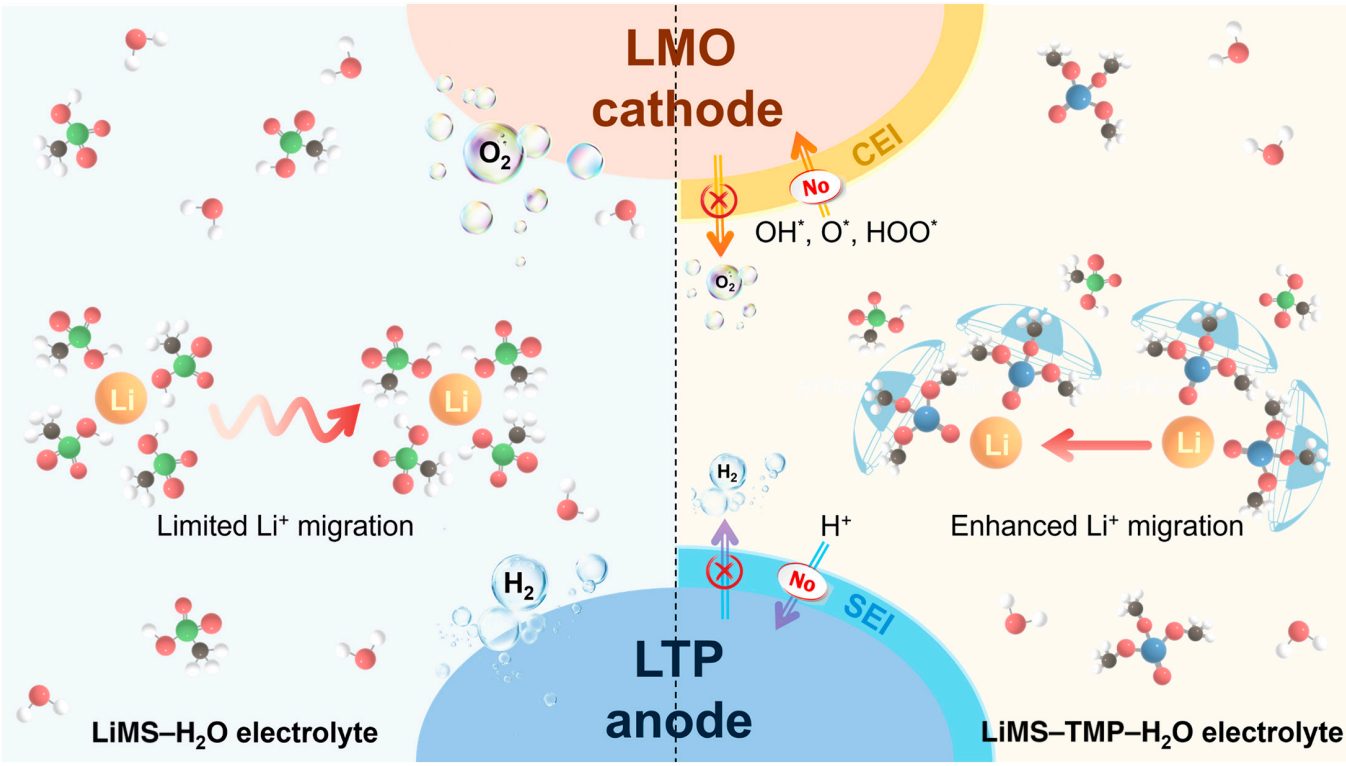



**Fig. 6.** Schematic diagram of simultaneously boosted liquid and interfacial $Li^+$ conduction in MIP electrolyte.

used 21-*m* WIS electrolyte for high-voltage aqueous batteries, such MIP electrolyte also provides wide operating temperature range (−40 to 25 °C) and superior cycling performance (>88% capacity retention after 1,000 cycles) in 2-A·h class pouch battery. The assembled 60-V, 15-A·h commercial LMO/LTP aqueous battery could drive an electric bike smoothly for a maximum distance of 70 km, demonstrating a breakthrough in replacing toxic lead–acid batteries in low-speed vehicles.

## Methods

### Materials and synthesis

LiMS–TMP–$H_2O$ electrolyte (1.1 *m*) was prepared by a mixture of LiMS ($LiCH_3SO_3$), deionized water, and TMP (>99%; Sigma-Aldrich). To synthesize $LiCH_3SO_3$, 14.45 g of methanesulfonate acid solution (70 wt % in water; Sigma-Aldrich) was dissolved in 50 ml of water and magnetic stirred at 80 °C when 2.4 g of lithium hydroxide (LiOH; reagent grade, 98%; Sigma-Aldrich) was added gradually. The solution was stirred at 80 °C for 2 h until all water evaporated. Finally, the product was collected and ground, followed by drying at 100 °C under vacuum overnight.

$TiO_2$ for battery test was synthesized as following method: 4 g of anatase $TiO_2$ (>99%; Sigma-Aldrich), 0.2 g of iron(III) oxide ($Fe_2O_3$; powder < 5 μm; Sigma-Aldrich), and 2 g of starch (from potato; Sigma-Aldrich) were mixed and ground for 15 min, followed by heated at 900 °C with a heating rate of 5 °C·$min^{-1}$ in argon for 4 h. The product was then stirred in 4 M HCl solution at 60 °C for 2 h and rinsed 3 times with deionized water to eliminate Fe ions. Finally, the product was dried at 80 °C overnight. LTP was prepared by sol–gel process and carbothermal reaction. Lithium dihydrogen phosphate ($LiH_2PO_4$; 24.6 kg, >99%; Aladdin), ammonium dihydrogen phosphate ($NH_4H_2PO_4$; 51.5 kg, >99%; Aladdin), $TiO_2$ (36.8 kg, >99%; Aladdin), and β-cyclodextrin (7.12 kg, >99%; Aladdin) were placed in a ball mill along with 180 kg of deionized water. The mixture was milled for 4 h to obtain a dispersed mixture with a solid content of 40%. Subsequently, the dispersed mixture was transferred to a sand mill using a diaphragm pump for ultrafine grinding. The high-speed sand milling process lasted for 4 h, resulting in a slurry with particle sizes controlled between 500 and 800 nm. The obtained slurry was then subjected to spray granulation in a spray granulator, maintaining an inlet temperature of 200 to 225 °C and an outlet temperature of 100 °C. This process yielded 108 kg of precursor material. The precursor material was then mixed uniformly with 10 kg of glucose (>99%; Aladdin) for 2.5 h. The mixture was then sintered at 800 °C under an argon atmosphere for 12 h at a rate of 10 °C·$min^{-1}$. Finally, the product was naturally cooled to room temperature, ground, and collected. ZnNbO was synthesized by a solid-state reaction method. Niobium(V) oxide ($Nb_2O_5$; 99.9%; Sigma-Aldrich) and zinc oxide (ZnO; >99%; Sigma-Aldrich) were mixed stoichiometrically and ball-milled at 800 rpm for 6 h, followed by calcinated in air at 1,200 °C for 6 h. The product was naturally cooled to room temperature, collected, and ground to obtain ZnNbO. LMO, $NCM_{111}$, and $NCM_{523}$ were purchased from MTI Corporation.

### Electrochemical measurements

CR2025 coin cells were assembled with cathode discs (diameter, 14 mm), absorbent glass mat separators (diameter,16 mm), and anode discs (diameter, 12 mm) as anode, and 125 μl of electrolyte was added. The composition of the electrodes is 70 wt % electrode material, 20 wt % acetylene black (AB; MTI Corporation), and 10 wt % polyvinylidene fluoride. The P/N ratio for the coin cell is 1.16. Pouch cells (100 mA·h) were assembled with one piece of LMO (>99%; MTI Corporation, single-side coating)

cathode piece (66 mm × 96 mm), absorbent glass mat (66 mm × 96 mm × 0.2 mm), one piece of LTP anode (single-side coating, 56 mm × 86 mm), with 10 to 15 g of electrolytes added per ampere-hour. The composition of cathode piece is 83.5 wt % LMO, 13 wt % AB, 2 wt % carboxymethyl cellulose (MTI Corporation), and 1.5 wt % styrene-butadiene rubber (MTI Corporation) on an aluminum foil as current collector, and the mass loading of cathode is about 35 mg·cm$^{-2}$. The composition of anode piece is 90 wt % LTP, 6 wt % AB, 2 wt % carboxymethyl cellulose, and 1.5 wt % styrene-butadiene rubber on an aluminum foil as current collector, and the mass loading of anode is 20 mg·cm$^{-2}$. The P/N value of the prepared cathode and anode is 1.73. The prepared cathode pieces, anode pieces, and separators were neatly stacked in the order of cathode–separator–anode and then fixed with adhesive tape. The cathode and anode leads were drawn out using an ultrasonic welding machine, and the welding points were covered with high-temperature tape to form a standard cell. The cell was then placed in a suitable aluminum–plastic film, and the premixed electrolyte was injected into the cell under vacuum at a mass of 10 to 15 g per ampere-hour. The pressure was maintained for 10 min, followed by heat sealing in vacuum to complete the battery fabrication process. The fabricated pouch cells were clamped with reinforcement plates for charge and discharge testing.

To assemble 2-A·h pouch cell, 8 pieces of LMO (>99%; MTI Corporation) cathode (185 mg·cm$^{-2}$, 140 mm × 67 mm, 12-μm-thick aluminum foil as current collector) and 7 pieces of LTP anode (160 mg·cm$^{-2}$, 137 mm × 63 mm, 12-μm-thick aluminum foil as current collector) were stacked with 9-μm-thick polypropylene separators (143 mm × 70 mm). The following fabrication process of 2-A·h pouch cell is the same as 100-mA·h pouch cell. To assemble an industrial-level 60-V, 15-A·h commercial LMO/LTP aqueous battery, 59 pieces of LMO (>99%; MTI Corporation) cathode (17.5 mg·cm$^{-2}$, 140 mm × 67 mm, 12-μm-thick aluminum foil as current collector) and 58 pieces of LTP anode (16.5 mg·cm$^{-2}$, 137 mm × 63 mm, 12-μm-thick aluminum foil as current collector) were firstly stacked with 9-μm-thick polypropylene separators (143 mm × 70 mm) to form a single cell. After adding 140 g of 1.1-*m* LiMS–TMP–$H_2O$ electrolyte, such single cell was sealed and aged 24 h before charge–discharge tests. The battery pack to drive electric bike is composed of 40 single cells connected in series. The electric bike test is conducted at 25 °C with a riding speed of approximately 25 km·h$^{-1}$. The total load was approximately 137.7 kg, including the electric bike's own weight (~77.7 kg, battery pack included) and the rider's weight (~60 kg).

The ESW was determined by linear sweep voltammetry at a scan rate of 10 mV·s$^{-1}$ using a BioLogic VMP3 workstation with a 3-electrode configuration. An Ag/AgCl electrode served as the reference, while a 316 stainless steel grid (200 mesh) functioned as both the working and counter electrodes. Prior to testing, all electrodes were ultrasonically cleaned in high-purity alcohol, rinsed 3 times with high-purity water, and dried. Measurements were carried out in a Swagelok T-type cell with a working electrode area of approximately 1 cm$^2$.

Cyclic voltammetry was conducted on the same workstation at a scan rate of 0.1 mV·s$^{-1}$. For cathode testing, the 3-electrode setup comprised active material (~2 mg) as the working electrode, a carbon rod as the counter electrode, and Ag/AgCl as the reference electrode. For anode testing, the working electrode consisted of active material (~1.5 mg), with a 2-mm platinum wire as the counter electrode and Ag/AgCl as the reference. Galvanostatic charge–discharge cycling was performed using a Neware battery tester under constant current mode at various current densities. The specific current densities corresponding to 1 C were 68 mA·g$^{-1}$ for LTO, 100 mA·g$^{-1}$ for LTP, and 200 mA·g$^{-1}$ for ZnNbO-based systems.

The $Li^+/H^+$ conductivity of $Li_3PO_4$ and LiF pellets was evaluated by EIS using an Admiral Instruments workstation, with a frequency range from 100 kHz to 100 mHz at 25 °C. Specifically, 500 and 100 mg of commercial γ-$Li_3PO_4$ (or LiF) powders were first hydraulically pressed into pellets with a diameter of 10 mm under applied loads of 4 and 8 tons, respectively, to fabricate millimeter-scale (around 2.1 mm in thickness) and micrometer-scale (350 to 980 μm in thickness) pellets for conductivity measurements. Then, the pellet was attached with wetted glass fiber (wetted by 1 M $Li_2SO_4$ solution) and then sandwiched between 2 stainless steel spacers to measure the EIS [74]. The $Li^+$ conductivity ($\sigma_{Li+}$) was calculated from $\sigma_{Li+} = l/RS$, where $R$ is the total impedance (from EIS result), $l$ is the sample thickness, and $S$ is the area (1.13 cm$^2$) [75]. To measure the $H^+$ conductivity of $Li_3PO_4$ and LiF pellets, the hydraulic pressed pellet was firstly attached with wetted glass fiber (wetted by 1 M $Li_2SO_4$ solution) and then sandwiched between 2 stainless steel spacers in a sealed chamber with wet $H_2$ (humidified 7% $H_2$ in Ar) atmosphere [76]. The $H^+$ conductivity ($\sigma_{H+}$) is obtained on the basis of the equation $\sigma_{H+} = \sigma_m - \sigma_{Li+}$, where $\sigma_m$ is the measured ionic conductivity of $Li_3PO_4$ (or LiF) pellets in $H_2$ atmosphere and $\sigma_{Li+}$ is $Li^+$ conductivity measured in air.

## Material characterization

FT-IR spectra were acquired using a Brüker Vertex 70 spectrometer over the wave number range of 400 to 4,000 cm$^{-1}$. Raman spectroscopy was conducted on a Horiba HR800 spectrometer in a backscattering configuration. This system, with a spectral resolution of 0.3 cm$^{-1}$, used a continuous-wave 633-nm HeNe laser (~1-mW maximum output) for both sample excitation and spectral collection. XPS measurements were performed on a Thermo Fisher Scientific ESCALAB 250 microprobe. Prior to analysis, sample surfaces were cleaned by $Ar^+$ sputtering under an argon partial pressure below $10^{-8}$ torr. Spectra were collected using a 200-μm x-ray beam (1,486.6 eV, 49.3 W), with binding energies referenced to the adventitious C 1s peak at 284.8 eV. All measurements were carried out under an ultrahigh vacuum (chamber pressure maintained at 2.0 nPa), and a wide survey scan (0 to 1,200 eV) was obtained for each sample to determine surface elemental composition. TEM was carried out using a Zeiss Libra 200MC instrument. Thermogravimetric analysis was performed using the TA Instruments Q500 in air from room temperature to 800 °C and from room temperature to 900 °C, respectively. An Agilent 8890 gas chromatography system, equipped with a CP-Molsieve 5-Å PT column and a thermal conductivity detector, was used to quantify $H_2$ evolution. The gas generated from the operating battery was channeled directly into the system's automatic sampling loop. High-purity argon was used as the carrier gas with a sampling interval of 15 min [77].

Water activity coefficient was obtained from a vapor–pressure measurement device [78]. Samples were put in a plastic container connected to a vacuum pump with a solution/free space ratio of 1:1. The container was degassed and flushed several times with Ar. After further purging with argon, the container was sealed, and the total pressure was measured with the time when the vapor is equilibrated with liquid phase. Before recording, a thermocouple was placed in the liquid to guarantee the temperature

(22 °C). The measurement assumed that the vapor originated from pure water, yielding a saturated vapor pressure of 2.69 kPa. This value was then applied in Raoult's law to calculate the corresponding water activity coefficient [79].

## Computational methodological details

### *MD simulations of electrolyte systems*

We applied MD simulations to investigate the structure and interactions of ion aggregates in lithium electrolytes with methanesulfonic acid lithium [Li($CH_3SO_3$), LiMS], $H_2O$, and TMP in different ratios. All MD simulations were carried out using the general AMBER force field [80]. First, geometry optimizations for MS and TMP were carried out at the HF/6-31G* level using Gaussian g09 [81] calculations. With Gaussian log file, we used antechamber to perform the restricted electrostatic potential fitting and produced the AMBER PREP files for MS and TMP, respectively. With the MS and TMP parameters ready, we constructed a $60 \times 60 \times 60$ $Å^3$ box that contains LiMS, transferable intermolecular potential 3P model $H_2O$, and TMP molecules in molar ratio as LiMS:$H_2O$:TMP = 1:3:$X$, $X = 0$, 2, 4, and 6, respectively. The MS, lithium ion, TMP, and $H_2O$ were randomly placed in the box using PACKMOL [82] and further processed using LEaP in AMBER18 package [83]. Each system is simulated with 3 copies. The details of MD simulations are shown in Table S5.

### *Simulation setups for electrolyte systems*

Each system went through energy minimization, 125-ps equilibration under isothermal–isovolumetric (NVT) ensemble with position restraint on solute component and a time step of 1 fs. The system continued to relax without restraint under isothermal–isobaric (NPT) ensemble using the AMBER18 package [83]. The NPT ensemble was used for further equilibration and MD production under 298 K, 1 bar, Langevin dynamics thermostat, and a time step of 2 fs. The simulations time in NPT ensemble are listed in Table S5 as 2,000 ns for each simulation. The particle mesh Ewald technique [84] was applied to calculate long-range electrostatic interactions. The short-range van der Waals and electrostatics were cut off at 12.0 Å with switch at 10.0 Å.

### *MD simulations of Li and proton diffusion in $Li_3PO_4$ interface systems*

The γ-$Li_3PO_4$ crystal structure in the *Pnma* space group (no. 62) is taken from Materials Project database [85,86] with unit cell parameters $a = 4.89$ Å, $b = 6.07$ Å, and $c = 10.42$ Å. The γ-$Li_3PO_4$ slab contains $6 \times 6 \times 2$ units ($36.426 \times 29.358 \times 20.832$ $Å^3$) with the (100) plane chosen as the solid–liquid interface. A transferable intermolecular potential 3P water box containing 3 M HCl and 3 M LiCl was built and put above the $Li_3PO_4$ slab. The whole $Li_3PO_4$–solution system contains 5,229 atoms and 903 $H_2O$ molecules in a periodic box of $36.426 \times 29.358 \times 57$ $Å^3$. Bonded and nonbonded parameters used for $PO_4^{3-}$ are displayed in Table S6. The "Zundel cation" kind $H^+$ parameter [87] was used, with the 12–6–4 parameter, $R_{min}/2$, modified to 0.841 Å (in Table S6). As studied in the paper of Li et al. [87], 3 $H^+$ types (the zundel cation, eigen cation, and $H_3O^+$) are parameterized. In the beginning of our interfacial systems, we carefully tested and evaluated the 3 $H^+$ models (all are parameterized as single spheres) and eventually derived the $H^+$ parameter for our study. First, the $H_3O^+$-type $H^+$ model (with $R_{min}/2$ parameter as 1.72 Å in the paper of Li et al.) describes a large ion–oxygen distance (IOD) of ~2.5 Å. In real-crystal $Li_3PO_4$ layer, $H^+$ is more easily to diffuse instead of bulky $H_3O^+$, which needs further dissociation of $H^+$ from $H_3O^+$. Thus, to describe the proton diffusion in slab instead of solution, the zundel cation-type $H^+$ or eigen cation-type $H^+$ with smaller $R_{min}/2$ parameters (0.925 and 0.841 Å, respectively) is better. However, our test simulation for eigen cation-type $H^+$ is very unstable. In addition, the origin zundel cation-type $H^+$ parameter generates an IOD distance of 1.3 Å. Eventually, the zundel cation-type $H^+$ parameters with the $R_{min}/2$ parameter modified to 1.841 Å are used in Table S6, which generate a reasonable IOD distance of ~1.25 Å (similar to the paper of Li et al. [87]).

The amorphous $Li_3PO_4$ was generated by rising the temperature to 2,000 to 2,500 K in MD simulation to accelerate the melting of crystal structure. After amorphous structure was formed, the system continues to be relaxed under 298 K. Each system is simulated with 3 copies. The message passing interface of AMBER18 package [83] is used to perform the minimization and MD simulations. Systems are relaxed under semi-isotropic pressure coupling (NPγT) ensemble (298 K, 1 bar) using Berendsen barostat and a time step of 1 fs. Same setups are used for long-range electrostatic interactions and short-range van der Waals and electrostatics as they are in the electrolyte systems. Similar setups to those in the electrolyte systems are used for energy minimization, followed by 125-ps equilibration under NVT ensemble with position restraint on the $Li_3PO_4$ slab. The simulations time in NPγT ensemble are listed in Table S5 as 200 ns for each simulation.

With the well-equilibrated systems, we further study the preference of $Li^+$ and $H^+$ diffusion in $Li_3PO_4$ slab. We generate vacant Li sites by removing random Li ions from the middle slab (yellow in Fig. 4A and B) and relax the system in 100-ps MD simulations; we call this process a "vacancy refilling" process. In general, 10 vacant Li sites are maintained in the beginning of a "vacancy refilling" process for γ-$Li_3PO_4$ and roughly 10 to 20 vacant Li sites for amorphous slab. The "vacancy refilling" process was repeated over 10 times in each simulation of 5 parallel copies. A summary of MD simulations is provided in Table S5.

### *PDOS calculations*

We performed a series of hybrid DFT calculations to obtain the PDOS using the Quickstep module of the CP2K program suite [88]. To prepare structures for the PDOS calculations, LiMS–$H_2O$ and 1.1-$m$ systems with over 1,000 atoms were equilibrized and relaxed in MD simulations for over 200 ns, which display similar coordination distribution with their corresponding large size systems. We extracted 10 configurations in 20-ns interval from the last 200 ns of each simulation; a total of 30 different configurations of 600 ns were used to generate the PDOS for each system. In Quickstep, a dual basis of localized Gaussians and plane waves is used to represent the Kohn–Sham equation and electronic density [89]. We used the molecularly optimized (MOLOPT) basis set with double-ζ plus polarization (DZVP-MOLOPT-GTH), as well as a planewave cutoff of 400 Ry and a REL_CUTOFF of 60 Ry. Hartree–Fock exchange (HFX) was applied with its efficient extension (the auxiliary density matrix method) [90], in which the contracted basis set with polarization function, cpFIT3, was applied as auxiliary basis set. The truncated HSE06 hybrid functional was adopted for the exchange correlation energy functional, where part of the exchange functional is replaced by HFX. Truncated Coulomb potential with cutoff radius less than half the cell was applied in the HFX calculation. The orbital transformation method is used in the self-consistent field wave function optimization cycle. The PDOSs

of different components were averaged over 30 different configurations of 600 ns to obtain a representative ensemble average.

### QM calculations

We performed QM calculations to study the reduction potential of TMP with and without Li using Gaussian g09 [81]. The initial TMP or TMP–Li structures were taken from MD simulation. The half-cell reactions of TMP with and without Li are expressed in Fig. 2A. We conducted QM calculations for each of the reactants and products in the half reactions at 298 K and 1 bar. Geometry optimization and frequency calculations were performed for each of the reactants and products using B3LYP-D3(BJ)/6-311G* with solvation model based on density continuum solvation model. B2PLYP-D3(BJ)/def2-TZVP was further used to obtain the single-point energy in gas phase, which was converted to gas-phase Gibbs free energy by adding with the thermal correction from the frequency calculations. M062X/6-31G* was used to obtain the solvation free energy in aqueous phase. The solvation model based on density continuum solvation model with water parameter ($\varepsilon = 78.3553$) and acetone ($\varepsilon = 20.493$), respectively, was applied during the geometry optimization and frequency calculations and to yield the solvation energy. The calculated thermochemistry values from Gaussian for each of the reactants and products were displayed in Table S7. The absolute Li/$Li^+$ electrode potential is approximately 1.4 V. The reduction potential of TMP-derived product versus Li/$Li^+$ electrode was calculated as [9,91,92],

$$E^0 = \left(\mathrm{vs}\frac{\mathrm{Li}^+}{\mathrm{Li}}\right) = E^0_{\mathrm{abs}} - E^0_{\mathrm{abs}}\left(\frac{\mathrm{Li}^+}{\mathrm{Li}}\right) = \frac{-\Delta G_{298\mathrm{K,solv}}}{nF} - 1.4 \quad (1)$$

where $F$ is the Faraday's constant and $n$ is the number of electrons (here, $n = 1$).

### Analysis of MD simulations

Data analysis of MD simulations was performed with AMBER [83,93] and GROMACS [94] built-in analysis tools, or visual molecular dynamics [95] and further generated using Matplotlib [96]. Structural features are shown by PyMOL (Schrödinger, LLC). The RDF defines the ratio of the average local number density of particles, $\langle\rho(r)\rangle$, at a distance $r$, to the bulk density of particles, $\rho$: $g(r) = \langle\rho(r)\rangle/\rho$. The self-diffusion coefficient $D$ for type A can be calculated from the mean-squared displacement (MSD) using the Einstein relation:

$$D = \frac{1}{2d}\lim_{t\to\infty}\frac{d}{dt}\langle \mathrm{MSD}(t)\rangle = \frac{1}{6}\lim_{t\to\infty}\frac{d}{dt}\left\langle [r(t)-r(0)]^2\right\rangle = \frac{1}{6}\lim_{t\to\infty}\frac{\sum_{i=1}^{N}\left\langle [r_i(t)-r_i(0)]^2\right\rangle_{i\in A}}{Nt} \quad (2)$$

where $d$ (=3) is the dimension of the system, $r_i$ represents the center-of-mass position of molecule $i$ at time $t$, $t = 0$ refers to a time reference point, and the angle brackets $\langle\ \rangle$ denote the ensemble average. Long MD trajectories were split into shorter trajectories from which the time reference points were updated, and then we average over all MSD values. The system-size dependency of self-diffusion of pure liquids is given by [97]:

$$D^0 = D^{\mathrm{MD}} + D^{\mathrm{FSC}} = D^{\mathrm{MD}} + \frac{2.837k_BT}{6\pi\eta L} \quad (3)$$

where $D^0$ is the diffusion in an infinitely large system, $D^{\mathrm{FSC}}$ is the finite-size correction, 2.837 is a dimensionless constant for a cubic simulation box with periodic boundary conditions, $\eta$ is the shear viscosity of the liquid, and $L$ is the length of the simulation box [97,98]. In equilibrium MD, the viscosity can be computed from the Green–Kubo relation or Einstein relation [99,100]. To obtain the off-diagonal stress tensors, we convert the AMBER prmtop and inpcrd files into GROMACS input files using the amb2gro_top_gro.py program and conducted MD simulations using the GROMACS 2019.4 package [94]. The off-diagonal components of the stress tensor were extracted using the gmx energy tool and processed using the Green–Kubo relation [99,100]. The accuracy of the calculated viscosity has been studied previously with the integration time, the early-time range to select reasonable viscosity, the size of the cubic box, and weight [97,101–103], which suggests that long integration time can improve the accuracy of the viscosity at the early-time range near 2 ps. We split long MD trajectories into shorter trajectories and examined different integration lengths and sampling frequencies [99]. The averaged shear viscosity at 6 to 50 ps is extracted from 200-ps calculations (100,000 iterations) before the shear viscosity difference keeps growing between trajectories. The simulated shear viscosity is also close to the experimental data (Fig. S61), verifying the accuracy of the simulation model.

The transference number is computed using the approach built upon concentrated solution theory [33,104,105]. The transport coefficients using the solvent reference are expressed in the Einstein form as:

$$W_{ij} = \frac{1}{6}\lim_{t\to\infty}\frac{d}{dt}\left\langle \frac{1}{n_i}\sum_a \Delta r^s_{i,a}(t)\cdot\frac{1}{n_j}\sum_\beta \Delta r^s_{j,\beta}(t)\right\rangle [\mathrm{SOL}] \quad (4)$$

where $i$ and $j$ represent different species and $n_i$ is the number of particles of species $i$. The superscript $s$ indicates that we use the average position of all solvent molecules in solution (SOL) as displacement reference. $\Delta r_{i,\alpha}{}^s(t)$ represents the displacement vectors for the motion of $\alpha$th particle of species $i$ from time 0 to $t$.

The cation transference number is computed as:

$$t_+{}^{\mathrm{SOL}} = \frac{W_{++} - W_{+-}}{W_{++} - 2W_{+-} + W_{--}} \quad (5)$$

The degree of uncorrelated ion motion ($\alpha$), or ionicity, is defined as the ratio of the actual total ionic conductivity ($\sigma$) and the ideal ionic conductivity ($\sigma_{\mathrm{NE}}$):

$$a = \frac{\sigma}{\sigma_{\mathrm{NE}}} = \frac{\sum_{i=1}^{N}\sum_{j=1}^{N} q_iq_j\left\langle \Delta\boldsymbol{r}_i(t)\Delta\boldsymbol{r}_j(t)\right\rangle}{\sum_{i=1}^{n} q_i^2\left\langle \Delta\boldsymbol{r}_i(t)^2\right\rangle} \quad (6)$$

The ratio represents the proportion of all the terms in the collective displacement to only the self-correlation term. When $\alpha = 1$ occurs, all ions move in completely uncorrelated motion. If $\alpha = 0$ occurs, it indicates that all of the cations only move together with anions. The correlations between the motion of ions ($\alpha$) were analyzed using the "atomiccorr" in "cpptraj" [93] from AMBER package.

DFT calculations for the analysis of binding energy between water and anions: DFT calculations were conducted under Gaussian 16 package. The B3LYP hybrid functional at 6-31g* level of basis set including the atom–pairwise dispersion (DFT-D3) correction with Becke–Johnson (BJ) damping to optimize geometry. Single-point calculation of every structure was carried

out at B3LYP/def2-TZVP including the DFT-D3 (BJ) correction. The binding energy was obtained by the following equation:

$$E_{binding} = E_{complex} - E_{anion} - E_{water} \quad (7)$$

## Acknowledgments

**Funding:** The work was supported by National Key R&D Program of China (2019YFA0709400), the National Natural Science Foundation of China (22288101, 21933010, and 22207108), and the Strategic Priority Research Program of Chinese Academy of Sciences (XDB37000000). The financial supports from Research Fund for International Excellent Young Scientists from National Natural Science Foundation of China (W2432039), Future Partner Network Project of CAS (030GJHZ2024073FN), and Director's Fund from Key Laboratory of Key Ceramic Materials-Free Exploration Project (E43GS1110G) are also acknowledged.
**Author contributions:** J.Z., G.L., and P.C. conceived and supervised the research. J.Z., Z.L., and M.H. prepared all samples. J.Z., Z.L., and M.H. carried out material and electrochemical characterizations. C.L. carried out all the theoretical simulations. Y.L. fabricated practical ampere-hour level aqueous batteries and conducted electric bike tests. J.Z., Z.L., and M.H. cowrote the manuscript. K.Y. and L.Z. finally checked the manuscript with valuable suggestions. J.Z., L.G., and P.C. supervised the work. All the authors contributed to discussions.
**Competing interests:** Y.L. and P.C. are the authors on 4 pending patent applications related to this work (CN 202111100900.X, 202110994266.2, 202111111817.2, and 202111100926.4). The authors declare that they have no other competing interests.

## Data Availability

All data are available in the manuscript or the Supplementary Materials or from the authors.

## Supplementary Materials

Figs. S1 to S61
Tables S1 to S7
Movies S1 and S2

## References

1. Whittingham MS. Lithium batteries and cathode materials. *Chem Rev*. 2004;104(10):4271–4302.
2. Grey CP, Tarascon JM. Sustainability and in situ monitoring in battery development. *Nat Mater*. 2017;16:45–56.
3. Goodenough JB, Kim Y. Challenges for rechargeable Li batteries. *Chem Mater*. 2010;22(3):587–603.
4. Xu K. Nonaqueous liquid electrolytes for lithium-based rechargeable batteries. *Chem Rev*. 2004;104(10):4303–4418.
5. Zhang H, Liu X, Li H, Hasa I, Passerini S. Challenges and strategies for high-energy aqueous electrolyte rechargeable batteries. *Angew Chem Int Ed Engl*. 2021;60(2):598–616.
6. Huang J, Guo Z, Ma Y, Bin D, Wang Y, Xia Y. Recent progress of rechargeable batteries using mild aqueous electrolytes. *Small Methods*. 2019;3(1):1800272.
7. Yamada Y, Wang J, Ko S, Watanabe E, Yamada A. Advances and issues in developing salt-concentrated battery electrolytes. *Nat Energy*. 2019;4:269–280.
8. Li M, Wang C, Chen Z, Xu K, Lu J. New concepts in electrolytes. *Chem Rev*. 2020;120(14):6783–6819.
9. Suo L, Borodin O, Gao T, Olguin M, Ho J, Fan X, Luo C, Wang C, Xu K. "Water-in-salt" electrolyte enables high-voltage aqueous lithium-ion chemistries. *Science*. 2015;350(6263):938–943.
10. Chen J, Fan X, Li Q, Yang H, Khoshi MR, Xu Y, Hwang S, Chen L, Ji X, Yang C, et al. Electrolyte design for LiF-rich solid–electrolyte interfaces to enable high-performance microsized alloy anodes for batteries. *Nat Energy*. 2020;5:386–397.
11. Yamada Y, Usui K, Sodeyama K, Ko S, Tateyama Y, Yamada A. Hydrate-melt electrolytes for high-energy-density aqueous batteries. *Nat Energy*. 2016;1:1–9.
12. Droguet L, Grimaud A, Fontaine O, Tarascon JM. Water-in-salt electrolyte (WiSE) for aqueous batteries: A long way to practicality. *Adv Energy Mater*. 2020;10(43):2002440.
13. Chen L, Zhang J, Li Q, Vatamanu J, Ji X, Pollard TP, Cui C, Hou S, Chen J, Yang C, et al. A 63 m superconcentrated aqueous electrolyte for high-energy Li-ion batteries. *ACS Energy Lett*. 2020;5(3):968–974.
14. Xu J, Ji X, Zhang J, Yang C, Wang P, Liu S, Ludwig K, Chen F, Kofinas P, Wang C. Aqueous electrolyte design for super-stable 2.5 V $LiMn_2O_4$ || $Li_4Ti_5O_{12}$ pouch cells. *Nat Energy*. 2022;7:186–193.
15. Pan J, Cheng Y-T, Qi Y. General method to predict voltage-dependent ionic conduction in a solid electrolyte coating on electrodes. *Phys Rev B*. 2015;91(13):Article 134116.
16. Ko J, Yoon YS. Recent progress in LiF materials for safe lithium metal anode of rechargeable batteries: Is LiF the key to commercializing Li metal batteries? *Ceram Int*. 2019;45(1):30–49.
17. Fuoss RM. Conductance of dilute solutions of 1-1 electrolytes[1]. *J Am Chem Soc*. 1959;81(11):2659–2662.
18. Xie J, Liang Z, Lu Y-C. Molecular crowding electrolytes for high-voltage aqueous batteries. *Nat Mater*. 2020;19:1006–1011.
19. Chen J, Vatamanu J, Xing L, Borodin O, Chen H, Guan X, Liu X, Xu K, Li W. Improving electrochemical stability and low-temperature performance with water/acetonitrile hybrid electrolytes. *Adv Energy Mater*. 2020;10(3):1902654.
20. Wang F, Borodin O, Ding MS, Gobet M, Vatamanu J, Fan X, Gao T, Eidson N, Liang Y, Sun W, et al. Hybrid aqueous/non-aqueous electrolyte for safe and high-energy Li-ion batteries. *Joule*. 2018;2(5):927–937.
21. Wang X, Yasukawa E, Kasuya S. Nonflammable trimethyl phosphate solvent-containing electrolytes for lithium-ion batteries: I. Fundamental properties. *J Electrochem Soc*. 2001;148(10):A1058.
22. Zhang L, Li J, Huang Y, Zhu D, Wang H. Synergetic effect of ethyl methyl carbonate and trimethyl phosphate on $BF_4^-$ intercalation into a graphite electrode. *Langmuir*. 2019;35(11):3972–3979.
23. Liu J, Yang C, Chi X, Wen B, Wang W, Liu Y. Water/Sulfolane hybrid electrolyte achieves ultralow-temperature operation for high-voltage aqueous lithium-ion batteries. *Adv Funct Mater*. 2022;32(1):2106811.
24. Zhang C, Ueno K, Yamazaki A, Yoshida K, Moon H, Mandai T, Umebayashi Y, Dokko K, Watanabe M. Chelate effects in glyme/lithium bis(trifluoromethanesulfonyl) amide solvate ionic liquids. I. Stability of solvate cations and correlation with electrolyte properties. *J Phys Chem B*. 2014;118(19):5144–5153.
25. Dorai A, Kuwata N, Taketawa R, Kawamura J, Katoaka K, Akimoto J. Diffusion coefficient of lithium ions in garnet-type

$Li_{6.5}La3Zr_{1.5}Ta_{0.5}O_{12}$ single crystal probed by $^{7}Li$ pulsed field gradient-NMR spectroscopy. *Solid State Ionics*. 2018;327:18–26.
26. Zhao G-J, Han K-L. Hydrogen bonding in the electronic excited state. *Acc Chem Res*. 2012;45(3):404–413.
27. Araujo CF, Coutinho JAP, Nolasco MM, Parker SF, Ribeiro-Claro PJA, Rudić S, Soares BIG, Vaz PD. Inelastic neutron scattering study of reline: Shedding light on the hydrogen bonding network of deep eutectic solvents. *Phys Chem Chem Phys*. 2017;19:17998–18009.
28. Clark JH, Green M, Madden RG. Strong hydrogen bonding between imidazole and trimethyl phosphate. *J Chem Soc Chem Commun*. 1983;136–137.
29. Tsubouchi S, Suzuki S, Nishimura K, Okumura T, Abe T. Effect of Lewis acids on graphite-electrode properties in EC-based electrolyte solutions with organophosphorus compounds. *J Electrochem Soc*. 2018;165(3):A680.
30. Khan, S. A., Khan S. B., Khan L. U., Farooq A., Akhtar K., Asiri A. M. Fourier transform infrared spectroscopy: Fundamentals and application in functional groups and nanomaterials characterization. *Handbook of materials characterization*. Cham: Springer; 2018. p. 317–344.
31. Huang S, Hou L, Li T, Jiao Y, Wu P. Antifreezing hydrogel electrolyte with ternary hydrogen bonding for high-performance zinc-ion batteries. *Adv Mater*. 2022;34(14):2110140.
32. Wang Y, Song LN, Wang XX, Wang YF, Xu JJ. Hydrogen-bonded organic frameworks-based electrolytes with controllable hydrogen bonding networks for solid-state lithium batteries. *Angew Chem Int Ed Engl*. 2024;63(41):Article e202401910.
33. Fang C, Mistry A, Srinivasan V, Balsara NP, Wang R. Elucidating the molecular origins of the transference number in battery electrolytes using computer simulations. *JACS Au*. 2023;3(2):306–315.
34. Zhang Q, Ma Y, Lu Y, Li L, Wan F, Zhang K, Chen J. Modulating electrolyte structure for ultralow temperature aqueous zinc batteries. *Nat Commun*. 2020;11:4463.
35. Ivanov-Shitz AK, Kireev VV. Growth and ionic conductivity of $Li_{3+}xP_{1-}xG_{e}xO_{4}$ ($x = 0.34$) single crystals. *Crystallogr Rep*. 2003;48:112–115.
36. Wan L, Liu T, Zhou X, Chen F. Improved electrochemical properties of $Li_{1.20}Mn_{0.54}Ni_{0.13}Co_{0.13}O_{2}$ cathode material with Li-conductive $Li_{3}PO_{4}$ coating and $F^{-}$ doping double modifications. *Powder Technol*. 2021;381:269–279.
37. Mousavi MPS, Dittmer AJ, Wilson BE, Hu J, Stein A, Bühlmann P. Unbiased quantification of the electrochemical stability limits of electrolytes and ionic liquids. *J Electrochem Soc*. 2015;162:A2250.
38. Tian Z, Guo W, Shi Z, Alhubail Z, Wang Y, Alsulaiman D, Zhu Y, Ming J, Sun J, Alshareef HN. The role of hydrogen bonding in aqueous batteries: Correlating molecular-scale interactions with battery performance. *ACS Energy Lett*. 2024;9(10):5179–5205.
39. Dubouis N, Lemaire L, Mirvaux B, Salager E, Deschamps M, Grimaud A. The role of the hydrogen evolution reaction in the solid–electrolyte interphase formation mechanism for "water-in-salt" electrolytes. *Energy Environ Sci*. 2018;11:3491–3499.
40. Suo L, Oh D, Lin Y, Zhuo Z, Borodin O, Gao T, Wang F, Kushima A, Wang Z, Kim HC, et al. How solid-electrolyte interphase forms in aqueous electrolytes. *J Am Chem Soc*. 2017;139(51):18670–18680.
41. Hou X, He X, Li J. Preparation and characterization of "water-in-salt" polymer electrolyte for lithium-ion batteries. *J Electrochem*. 2021;27(2):202–207.
42. Wang Y, Zhang F, Chen JA, Zhang X, Wen J, Wang C, Huang G. Carbon-coated $LiTi_{2}(PO_{4})_{3}$ composites synthesized through tannic acid with high rate performance for aqueous lithium-ion batteries. *J Alloys Compd*. 2023;939:Article 168704.
43. Zhou Z, Li Y, Xia M, Zhou N. Enhancing the electrochemical properties of $LiTi_{2}(PO_{4})_{3}$/C anode for aqueous rechargeable lithium battery by Li vacancy. *Solid State Ionics*. 2018;315:1–6.
44. Zhou N, Huang S, Hong T, Luo W, Tian Y, Lu X, Zhou Z. High-performance $LiTi_{2}(PO_{4})_{3}$@carbon anode using double carbon sources for aqueous lithium ion battery. *Ceram Int*. 2017;43(12):9327–9333.
45. He Z, Jiang Y, Sun D, Dai L, Wang H. Advanced $LiTi_{2}(PO_{4})_{3}$/C anode by incorporation of carbon nanotubes for aqueous lithium-ion batteries. *Ionics*. 2017;23:575–583.
46. Bruce FNO, He R, Xuan R, Xin B, Ma Y, Li Y. An experimental and kinetic modeling study of the auto-ignition delay times of trimethyl phosphate-in-air mixtures. *Appl Energy Combust Sci*. 2024;17:Article 100237.
47. Zhu D, Ren Y, Yu Y, Zhang L, Wan Y, Wang H, Gao W, Han B, Zhang L. Flame-retardant additive/co-solvent contained in organic solution for safe second batteries: A review. *ChemElectroChem*. 2023;10(8):Article e202300009.
48. Korobeinichev OP, Rybitskaya IV, Shmakov AG, Chernov AA, Bolshova TA, Shvartsberg VM. Mechanism of inhibition of hydrogen/oxygen flames of various compositions by trimethyl phosphate. *Kinet Catal*. 2010;51:154–161.
49. Korobeinichev OP, Bolshova T, Bolshova TA, Shmakov AG, Shvartsberg VM. Skeletal mechanism of inhibition and suppression of a methane-air flame by addition of trimethyl phosphate. *Combust Explos Shock Waves*. 2014;50:130–134.
50. Li W, Dahn JR, Wainwright DS. Rechargeable lithium batteries with aqueous electrolytes. *Science*. 1994;264:1115–1118.
51. Wang H, Huang K, Zeng Y, Yang S, Chen L. Electrochemical properties of $TiP_{2}O_{7}$ and $LiTi_{2}(PO_{4})_{3}$ as anode material for lithium ion battery with aqueous solution electrolyte. *Electrochim Acta*. 2007;52(5162):3280–3285.
52. Suo L, Borodin O, Sun W, Fan X, Yang C, Wang F, Gao T, Ma Z, Schroeder M, von Cresce A, et al. Advanced high-voltage aqueous lithium-ion battery enabled by "water-in-bisalt" electrolyte. *Angew Chem*. 2016;128(25):7252–7257.
53. Zhu X, Mao M, Lin Z, Yue J, Li M, Lv T, Zhou A, Hu Y-S, Li H, Huang X, et al. Wadsley-Roth phase niobium-based oxide anode promising high power and energy density aqueous Li-ion batteries. *ACS Mater Lett*. 2022;4(9):1574–1583.
54. Ping J, Rauf S, Tayyab Z, Yang C. Electrochemical performance of spherical $LiCoO_{2}$ with high stability in neutral aqueous electrolyte. *Ceram Int*. 2021;47(12):16460–16466.
55. Ramanujapuram A, Gordon D, Magasinski A, Ward B, Nitta N, Huang C, Yushin G. Degradation and stabilization of lithium cobalt oxide in aqueous electrolytes. *Energy Environ Sci*. 2016;9:1841–1848.
56. Lee C, Miyahara Y, Abe T, Miyazaki K. Electrochemical properties of Ni-rich $LiNi_{x}Co_{y}Mn_{z}O_{2}$ materials for use in aqueous lithium-ion batteries: How do they differ from those in non-aqueous systems? *J Power Sources*. 2022;524:Article 231081.
57. Zhou Y, Wang Z, Lu YC. Flexible aqueous lithium-ion batteries with ultrahigh areal capacity and long cycle life. *Mater Today Energy*. 2021;19:Article 100570.

58. Wang Y, Wang T, Bu S, Zhu J, Wang Y, Zhang R, Hong H, Zhang W, Fan J, Zhi C. Sulfolane-containing aqueous electrolyte solutions for producing efficient ampere-hour-level zinc metal battery pouch cells. *Nat Commun*. 2023;14:1828.
59. Wu H, Hao J, Jiang Y, Jiao Y, Liu J, Xu X, Davey K, Wang C, Qiao SZ. Alkaline-based aqueous sodium-ion batteries for large-scale energy storage. *Nat Commun*. 2024;15:575.
60. Chen L, Cao L, Ji X, Hou S, Li Q, Chen J, Yang C, Eidson N, Wang C. Enabling safe aqueous lithium ion open batteries by suppressing oxygen reduction reaction. *Nat Commun*. 2020;11:2638.
61. Zhou A, Liu Y, Zhu X, Li X, Yue J, Ma X, Gu L, Hu YS, Li H, Huang X, et al. $TiO_2$(B) anode for high-voltage aqueous Li-ion batteries. *Energy Storage Mater*. 2021;42:438–444.
62. Zhang J, Cui C, Wang PF, Li Q, Chen L, Han F, Jin T, Liu S, Choudhary H, Raghavan SR, et al. "Water-in-salt" polymer electrolyte for Li-ion batteries. *Energy Environ Sci*. 2020;13:2878–2887.
63. Hou Z, Mao W, Zhang Z, Chen J, Ao H, Qian Y. Bipolar electrode architecture enables high-energy aqueous rechargeable sodium ion battery. *Nano Res*. 2022;15:5072–5080.
64. Jiang L, Liu L, Yue J, Zhang Q, Zhou A, Borodin O, Suo L, Li H, Chen L, Xu K, et al. High-voltage aqueous Na-ion battery enabled by inert-cation-assisted water-in-salt electrolyte. *Adv Mater*. 2020;32(2):1904427.
65. Zhou A, Zhang J, Chen M, Li X, Li S, Ma J, Lv T, Zhu X, Feng G, Suo L. Interface preconstruction enables robust passivation of the ah-level aqueous Li-ion batteries. *J Am Chem Soc*. 2025;147(14):11811–11820.
66. Li S, Shang Y, Ren X, Zhao A, Chen N, Li L, Wu F, Chen R. Strengthened O–H bonds in an aqueous electrolyte for nonflammable Li-ion batteries. *ACS Nano*. 2025;19(17):16584–16596.
67. Hou C, Ke C, Chen R, Lin Y, Huang Q, Liu S, Wang J. A 2.6 m aqueous electrolyte for high-energy-density lithium-ion pouch cells using $NbO_2$ anode. *ACS Energy Lett*. 2025;11(1):654–663.
68. Zhou A, Chen Q, Zhu X, Dan D, Li S, Li X, Ma J, Lv T, Hu Z, Zhang C, et al. Aquatic environment breaks the size confinement of the $TiO_2$ anodes in aqueous batteries. *Angew Chem Int Ed Engl*. 2025;65(1):Article e20365.
69. Huang Y, Lu K, Dong J, Wang X, Li J, Gong Z, He Y, Jia H, Yuan G, Wang P, et al. Chelate reconstruction with a $H_2O$-poor and zinc-rich interface toward robust anti-corrosion Ah-level zinc aqueous batteries. *Energy Storage Mater*. 2025;84:Article 104821.
70. Lv W, Tan Y, Guo C, He X, Zeng L, Zhu J, Yang L, Chen Z, Yin X, Xu J, et al. Triple regulation of water molecules behavior to realize high stability and broad temperature tolerance in aqueous zinc metal batteries via a novel cost-effective eutectic electrolyte. *Adv Energy Mater*. 2025;15(15):2403689.
71. Wang GJ, Yang LC, Qu QT, Wang B, Wu YP, Holze R. An aqueous rechargeable lithium battery based on doping and intercalation mechanisms. *J Solid State Electrochem*. 2010;14:865–869.
72. Wang F, Lin Y, Suo L, Fan X, Gao T, Yang C, Han F, Qi Y, Xu K, Wang C. Stabilizing high voltage $LiCoO_2$ cathode in aqueous electrolyte with interphase-forming additive. *Energy Environ Sci*. 2016;9(12):3666–3673.
73. Wang Y, Yang SZ, You Y, Feng Z, Zhu W, Gariépy V, Xia J, Commarieu B, Darwiche A, Guerfi A, et al. High-capacity and long-cycle life aqueous rechargeable lithium-ion battery with the $FePO_4$ anode. *ACS Appl Mater Interfaces*. 2018;10(8):7061–7068.
74. Hao J, Li B, Li X, Zeng X, Zhang S, Yang F, Liu S, Li D, Wu C, Guo Z. An in-depth study of Zn metal surface chemistry for advanced aqueous Zn-ion batteries. *Adv Mater*. 2020;32(34):2003021.
75. Wang Z, Hu J, Han L, Wang Z, Wang H, Zhao Q, Liu J, Pan F. A MOF-based single-ion $Zn^{2+}$ solid electrolyte leading to dendrite-free rechargeable Zn batteries. *Nano Energy*. 2019;56:92–99.
76. Pornprasertsuk R, Kosasang O, Somroop K, Horprathum M, Limnonthakul P, Chindaudom P, Jinawath S. Proton conductivity of Y-doped $BaZrO_3$: Pellets and thin films. *Solid State Sci*. 2011;13(7):1429–1437.
77. Kao C-C, Ye C, Hao J, Shan J, Li H, Qiao SZ. Suppressing hydrogen evolution via anticatalytic interfaces toward highly efficient aqueous Zn-ion batteries. *ACS Nano*. 2023;17(4):3948–3957.
78. Guendouzi ME, Mounir A, Dinane A. Water activity, osmotic and activity coefficients of aqueous solutions of $Li_2SO_4$, $Na_2SO_4$, $K_2SO_4$,$(NH_4)_2SO_4$, $MgSO_4$, $MnSO_4$, $NiSO_4$, $CuSO_4$, and $ZnSO_4$ at $T$=298.15 K. *J Chem Thermodyn*. 2003;35(2):209–220.
79. Miyawaki O, Saito A, Matsuo T, Nakamura K. Activity and activity coefficient of water in aqueous solutions and their relationships with solution structure parameters. *Biosci Biotechnol Biochem*. 1997;61:466–469.
80. Wang J, Wolf RM, Caldwell JW, Kollman PA, Case DA. Development and testing of a general amber force field. *J Comput Chem*. 2004;25(9):1157–1174.
81. Gaussian 09, *Revision A.01*. Wallingford (CT): Gaussian, Inc.; 2009.
82. Martínez L, Andrade R, Birgin EG, Martínez JM. PACKMOL: A package for building initial configurations for molecular dynamics simulations. *J Comput Chem*. 2009;30(13):2157–2164.
83. Case DA, Ben-Shalom I, Brozell SR, Cerutti DS, Cheatham T, Cruzeiro VWD, Darden T, Duke RE, Ghoreishi D, Gilson MK. *AMBER 2018*. CA: University of California; 2018.
84. Darden T, York D, Pedersen L. Particle mesh Ewald - An *N*. log(*N*) method for Ewald sums in large systems. *J Chem Phys*. 1993;98:10089–10092.
85. Jain A, Ong SP, Hautier G, Chen W, Richards WD, Dacek S, Cholia S, Gunter D, Skinner D, Ceder G, et al. Commentary: The materials project: A materials genome approach to accelerating materials innovation. *APL Mater*. 2013;1:Article 011002.
86. de Jong M, Chen W, Angsten T, Jain A, Notestine R, Gamst A, Sluiter M, Krishna Ande C, van der Zwaag S, Plata JJ, et al. Charting the complete elastic properties of inorganic crystalline compounds. *Sci Data*. 2015;2:Article 150009.
87. Li P, Song LF, Merz KM Jr. Systematic parameterization of monovalent ions employing the nonbonded model. *J Chem Theory Comput*. 2015;11(4):1645–1657.
88. Kühne TD, Iannuzzi M, del Ben M, Rybkin VV, Seewald P, Stein F, Laino T, Khaliullin RZ, Schütt O, Schiffmann F, et al. CP2K: An electronic structure and molecular dynamics software package - Quickstep: Efficient and accurate electronic structure calculations. *J Chem Phys*. 2020;152:Article 194103.

89. VandeVondele J, Krack M, Mohamed F, Parrinello M, Chassaing T, Hutter J. Quickstep: Fast and accurate density functional calculations using a mixed Gaussian and plane waves approach. *Comput Phys Commun*. 2005;167:103–128.
90. Guidon M, Hutter J, VandeVondele J. Auxiliary density matrix methods for Hartree−Fock exchange calculations. *J Chem Theory Comput*. 2010;6(8):2348–2364.
91. Ho J, Coote ML, Cramer C, Truhlar DG. *Organic Electrochemistry, Fifth Edition 229–260*. USA: CRC Press; 2015.
92. Borodin O, Behl W, Jow TR. Oxidative stability and initial decomposition reactions of carbonate, sulfone, and alkyl phosphate-based electrolytes. *J Phys Chem C*. 2013;117(17):8661–8682.
93. Roe DR, Cheatham TE. PTRAJ and CPPTRAJ: Software for processing and analysis of molecular dynamics trajectory data. *J Chem Theory Comput*. 2013;9(7):3084–3095.
94. Berendsen HJC, Vanderspoel D, Vandrunen R. Gromacs - A message-passing parallel molecular-dynamics implementation. *Comput Phys Commun*. 1995;91(1–3):43–56.
95. Humphrey W, Dalke A, Schulten K. VMD: Visual molecular dynamics. *J Mol Graph Model*. 1996;14(1):33–38.
96. Hunter JD. Matplotlib: A 2D graphics environment. *Comput Sci Eng*. 2007;9(3):90–95.
97. Yeh I-C, Hummer G. System-size dependence of diffusion coefficients and viscosities from molecular dynamics simulations with periodic boundary conditions. *J Phys Chem B*. 2004;108(40):15873–15879.
98. Jamali SH, Hartkamp R, Bardas C, Söhl J, Vlugt TJH, Moultos OA. Shear viscosity computed from the finite-size effects of self-diffusivity in equilibrium molecular dynamics. *J Chem Theory Comput*. 2018;14(11):5959–5968.
99. Bedrov D, Smith GD, Sewell TD. Temperature-dependent shear viscosity coefficient of octahydro-1,3,5,7-tetranitro-1,3,5,7-tetrazocine (HMX): A molecular dynamics simulation study. *J Chem Phys*. 2000;112:7203–7208.
100. Daivis PJ, Evans DJ. Comparison of constant pressure and constant volume nonequilibrium simulations of sheared model decane. *J Chem Phys*. 1994;100:541–547.
101. Mouas M, Gasser JG, Hellal S, Grosdidier B, Makradi A, Belouettar S. Diffusion and viscosity of liquid tin: Green-Kubo relationship-based calculations from molecular dynamics simulations. *J Chem Phys*. 2012;136:Article 094501.
102. Mondello M, Grest GS. Viscosity calculations of n-alkanes by equilibrium molecular dynamics. *J Chem Phys*. 1997;106(22):9327–9336.
103. Zhang Y, Otani A, Maginn EJ. Reliable viscosity calculation from equilibrium molecular dynamics simulations: A time decomposition method. *J Chem Theory Comput*. 2015;11(8):3537–3546.
104. Wheeler DR, Newman J. Molecular dynamics simulations of multicomponent diffusion. 1. Equilibrium method. *J Phys Chem B*. 2004;108(47):18353–18361.
105. Fong KD, Bergstrom HK, McCloskey BD, Mandadapu KK. Transport phenomena in electrolyte solutions: Nonequilibrium thermodynamics and statistical mechanics. *AICHE J*. 2020;66(12):Article e17091.
106. Manalastas W Jr, Kumar S, Verma V, Zhang L, Yuan D, Srinicasan M. Water in rechargeable multivalent-ion batteries: An electrochemical Pandora's box. *ChemSusChem*. 2019;12(2):379–396.